J. Fluid Mech. (1996), *vol.* 327, *pp.* 221–254

Simulation of plunging wave impact on a vertical wall

By SHEGUANG ZHANG†, DICK K. P. YUE‡ AND KATSUJI TANIZAWA¶

Department of Ocean Engineering, Massachusetts Institute of Technology, Cambridge,
MA 02139, USA

(Received 19 June 1995 and in revised form 10 April 1996)

We present a numerical study of the impact of a two-dimensional plunging wave on a rigid vertical wall in the context of potential flow. The plunging wave impinging the wall is generated using a mixed-Eulerian–Lagrangian (MEL) boundary-integral scheme. The initial stage of the impact is characterized by an oblique impact of a liquid wedge on the wall and is solved using a similarity solution. Following the initial impact, the MEL simulation is continued to capture the transient impact process. The effect of an air cushion trapped between the plunger and the wall is considered. In addition to details such as temporal evolutions and surface profiles, the main interests are the maximum impact pressure on the wall and its rise time. To arrive at appropriate scaling laws for these, simulations are performed and correlations are explored for a broad range of local plunging wave kinematic and geometric parameters. To assess the present results, direct comparisons are made with the experiment of Chan & Melville (1988). Reasonable quantitative agreement is obtained and likely sources for discrepancies are identified and discussed.

1. Introduction

Large pressures and loads associated with breaking wave impact on sea walls, ships and offshore structures are important subjects in ocean engineering. The magnitudes of the impact pressure maxima are related to the type of breaking waves, among which plunging breakers usually produce the largest impact pressures on the structures. In this paper, the impact of a plunging breaker on a rigid vertical wall is considered.

Both field measurements (Miller, Leverette & O'Sollivan 1974; Blackmore & Hewson 1984; Führböter 1986; Whillock 1987) and model experiments (Bagnold 1939; Hayashi & Hattori 1958; Kirkgöz 1990, 1991; Schmidt, Oumeraci & Partenscky 1992; Oumeraci, Klammer & Partenscky 1993; Hattori, Arami & Yui 1994, for impact of shallow-water breaking waves; Chan & Melville 1988, Chan 1994, for impact of deep-water breaking waves) have shown that the impact pressure history due to a plunging breaker striking a vertical wall is of high intensity (10 ~ 100 kPa) and short duration ($10^{-1} \sim 10^{-3}$ s). One mechanism responsible for the generation of high pressure intensities is attributed to the direct collision of the fluid body in the region of the plunger tip and the wall surface (Lundgren 1969; Schmidt *et al.*

---

† Present address: Ship Technology Division, SAIC, Annapolis, MD 21401, USA.

‡ Author to whom correspondence should be directed.

¶ Present address: Ship Research Institute, Shinkawa, Mitaka, Tokyo, Japan.

1992). In this process, the velocity of the fluid and the effective fluid mass involved in the impact directly contribute to the generation of the pressure maxima on the wall. Another mechanism is related to the effect of an air cushion trapped between the concave boundary of the plunger surface and the wall (Bagnold 1939). As the plunger impinges on the wall, the trapped air pocket is compressed, which induces a large pressure gradient in the adjacent fluid as well as a high pressure on the wall. Researchers (Hayashi & Hattori 1958; Chan & Melville 1988; Hattori *et al.* 1994) found that enclosure of the air pocket during the plunger impact tends to increase the impact pressure maxima and reduce the time required for the impact pressure to reach a maximum value. Furthermore, they found that, under similar impact conditions, an impact with a smaller initial air pocket volume tends to produce larger impact pressures. In addition to its effect on the pressure maxima, the trapped air interacts with the surrounding fluid in a pulsating motion wherein the fluid energy is alternately stored and released. This causes high-frequency oscillations in the impact pressure history (Schmidt *et al.* 1992) which is typically modulated by a damping mechanism associated with leakage of the trapped air (Mitsuyasu 1966) and disintegration of the air pocket into a mixture of bubbly flow (Cooker & Peregrine 1991).

These studies also show that the measured magnitude and rise time of the impact pressure maxima are marked by large scatter and lack of repeatability even under nearly identical experimental conditions. Furthermore, they are highly sensitive to local impact conditions, such as the inclination angle and position of the wall relative to the approaching breaker (e.g. Whillock 1987; Kirkgöz 1990, 1991; Chan & Melville 1988).

Significantly, effective scaling laws for extrapolating from model to prototype scales are as yet unavailable (e.g. Führböter 1986), in large part due to the lack of understanding of mechanisms associated with the trapped air. Bagnold (1939) presented a piston model to approximate the trapped-air impact process as an adiabatic compression of a column of fluid mass in an air-filled rigid cylinder. His model correlates the impact pressure maxima with the ratio of the length of the column of the 'kinetic mass' of water to the thickness of the air pocket. Führböter (1986) pointed out that different parameters, and hence scaling laws, must be employed in different flow regions in the impact process. Stive (1984) indicated that the parameter $P_0/\rho U^2$ must be scaled if the deceleration of the water after impact is governed by the compression of the enclosed air. Here, P_0 is the initial air (atmospheric) pressure in the air pocket, ρ the fluid density, and U the (initial) impact velocity of breaking waves normal to the wall. A number of other scaling criteria have also been proposed in wave-impact and water-entry problems (Whitman & Pancione 1973; see also summaries in Hayashi & Hattori 1958; Stive 1984; Blackmore & Hewson 1984).

Although many experimental studies on breaking wave impact have been performed, few corresponding analytical and numerical studies are available due to the highly nonlinear and transient nature of the problem. The essential physics involved in the impact process can be captured in the simplified theoretical framework of potential flow. Compressibility of the fluid is ignored in view of the fact that the impacting plunging breaker is wedge-like as it strikes the wall and that the impact velocity is much less than the speed of sound in the fluid (Korobkin & Pukhnachov 1988). Furthermore, viscosity and surface tension effects can be neglected since inertia forces are dominant during the impact (Cooker & Peregrine 1991).

In this context, numerical simulations were performed by Vinje & Brevig (1980, 1981) who employed a mixed-Eulerian–Lagrangian (MEL) boundary-integral method to calculate the forces on solid bodies due to plunging breaker impact. Owing to difficulties in evaluating the impact pressures, particularly at the initial stage of the impact, the forces were obtained by calculating the time derivative of the pressure impulse. Using classical impulse theory (Lamb 1932) and the MEL boundary-integral method of Dold & Peregrine (1986), Cooker & Peregrine (1992, 1995) obtained the pressure impulse due to a breaking wave striking a vertical wall. In their study, the breaking wave approaches the wall in such a way that the waterline quickly moves up along the wall, as a result of which no direct collision occurs between the wave front and the wall. Their theory was used by Chan (1994) to compare with experiments, and it was extended by Topliss (1994) to cases involving wave sloshing in a container, and wave impact with entrained air and its effect on a flexible wall. Since these studies rely on the impulse theory, they do not provide a complete description of the impact process and require *ad hoc* parameters to estimate the size of the impact area and the duration of the impact. Note that other numerical methods such as the volume of fluid method (e.g. Wang & Su 1992) have also been used to study breaking wave impact. However, these fixed-domain methods need much more computing effort to provide the necessary resolution of the spatial and temporal scales of the trapped air.

In reviewing the previous studies, it is noted that a number of important questions associated with the plunging wave impact problem remain unresolved. For instance: (i) How can the initial stage of the plunger impingement on the wall be properly characterized and simulated? (ii) What are the most important scaling parameters governing the trapped-air wave impact process? (iii) How do the maximum value and duration of the impact pressure scale with these parameters? By performing high-resolution simulations of trapped-air plunging wave impact and direct comparison to experiments, the aim of this study is to provide some information to help in answering these open questions.

In this study, potential flow theory is used to investigate the impact of a two-dimensional plunging breaker on a vertical rigid wall. A computational tank is used which consists of a piston wave maker at one end, a rigid vertical wall on the other end, and has constant initial water depth. By prescribing the motions of the piston wave maker, a (deep-water) plunging wave is created at the opposite wall. The simulation is based on the MEL boundary-integral scheme of Vinje & Brevig (1981) which has been shown to obtain high-accuracy comparisons to experiments in a similar set-up (Dommermuth *et al.* 1988).

The initial stage of the impact must be treated with some care. If a small portion of the breaker tip is allowed to pass through the wall and is then cut off to produce a finite wetted area on the wall, the subsequent simulation results in a non-physically high spike in the impact pressure (and in a non-smooth surface profile) which fails to converge with finer temporal and spatial discretizations (cf. Tanizawa & Yue 1991, 1992). To circumvent this difficulty, and to better characterize the initial stage of the impact, a (small-time) similarity solution for the general oblique impact of a liquid wedge on a wall is obtained. This solution extends the work of Borisova, Koriavov & Moiseev (1959) (see also Cumberbatch 1960) who considered the case of symmetric normal impact. Such a patching allows a smooth continuation of the MEL simulation and a convergent pressure history. Assuming adiabatic conditions, the effect of the trapped air is modelled using a polytropic gas law. With appropriate treatment of the spray roots (e.g. Zhao & Faltinsen 1993), the MEL simulations can be carried out through a number of oscillations of the air pocket (see figures 17 and 18).

By varying the parameters of the problems such as piston motions and tank length, a set of simulations is carried out corresponding to a wide range of local impact parameters such as impact velocity and aspect ratio of the initial air pocket (see

Appendix B). In each case, the maximum value of the impact pressure on the wall, P_m, and its rise time, T_r (time from the instant of the initial impact to the instant when P_m is reached) are obtained and correlated with the impact parameters. Based on these results, a scaling model, which is a generalization of Bagnold's piston model, is proposed and the empirical parameters of the model are determined.

Finally, to evaluate the simulation and the scaling model, a direct calculation is performed for the conditions of a plunging wave impact on a vertical wall considered in the experiment of Chan & Melville (1988). The comparisons show reasonable quantitative agreements. Likely causes for some of the discrepancies are also identified and discussed.

In the following, a brief statement of the problem is given in §2. The modelling of the initial stage of the impact is presented in §3. The numerical simulation beyond the initial impact is given in §4. These results are used to propose scaling laws which are discussed in §5. A direct comparison with the experiment of Chan & Melville (1988) is provided in §6, and some concluding remarks are made in §7. The derivation of the similarity solution for the general oblique impact of a liquid wedge is given in Appendix A and details of the plunger wave characteristics used in this study are presented in Appendix B.

2. Statement of the problem

The simulation of a plunging wave impacting a vertical wall can be divided into three stages: (i) the generation of the plunger to the point just before the impact ($0 \leqslant t < t_I$); (ii) the initial stage of the impact (from the instant $t = t_I$ when the plunger tip touches the wall, to the instant $t = t_I + \Delta t_I$ just after the converging plunger jet tip converts into a diverging jet spreading along the wall); and (iii) the subsequent evolution ($t > t_I + \Delta t_I$) involving a trapped air pocket. In the present approach, the direct MEL simulations are carried out for the stages before and after the initial impact, and a similarity solution is derived and used for the initial impact stage (ii).

Definition sketches corresponding to stages (i) and (iii) are shown in figures 1(*a*) and 1(*b*) respectively. The fluid flow in a rectangular numerical tank of length L_0 and initial water depth h_0 is described by Cartesian coordinates (x,y) and time t. The origin of the coordinate system is located at the intersection between the still water level ($y = 0$) and the y-axis which is directed vertically up. A piston wave maker, S_L, is located at $x = 0$ initially, and a rigid wall, S_R, is on the right-hand end of the tank at $x = L_0$. The bottom of the tank and the free surface are denoted as S_B and S_f, respectively. Unless otherwise noted, we non-dimensionalize the problem hereafter by selecting mass, length and time units such that the fluid density $\rho \equiv 1$, the gravitational acceleration $g \equiv 1$, and initial tank depth $h_0 \equiv 1$.

At $t = 0$, the piston wave maker S_L moves abruptly from rest to a constant velocity U_0. It travels a distance L_1 and then stops. Owing to the phase focusing of the different frequency components, a plunging breaker is created towards the far wall. To provide an additional adjustment of the characteristics of the resulting breaking wave (see Appendix B), a channel of length L_e and height h_e at the bottom of S_R is opened at $t = 0$, maintained up to the instant of impact t_I, and is closed thereafter. For definiteness, we fix $L_e = L_0/5$, and set the horizontal exit velocity in the channel to be uniform given by $U_e = (10y_R)^{1/2}$, where y_R is the height of the water line on S_R. The channel height h_e is left as a parameter of the simulation to be adjusted. This is a convenient procedure to create trapped air pockets of different sizes and at

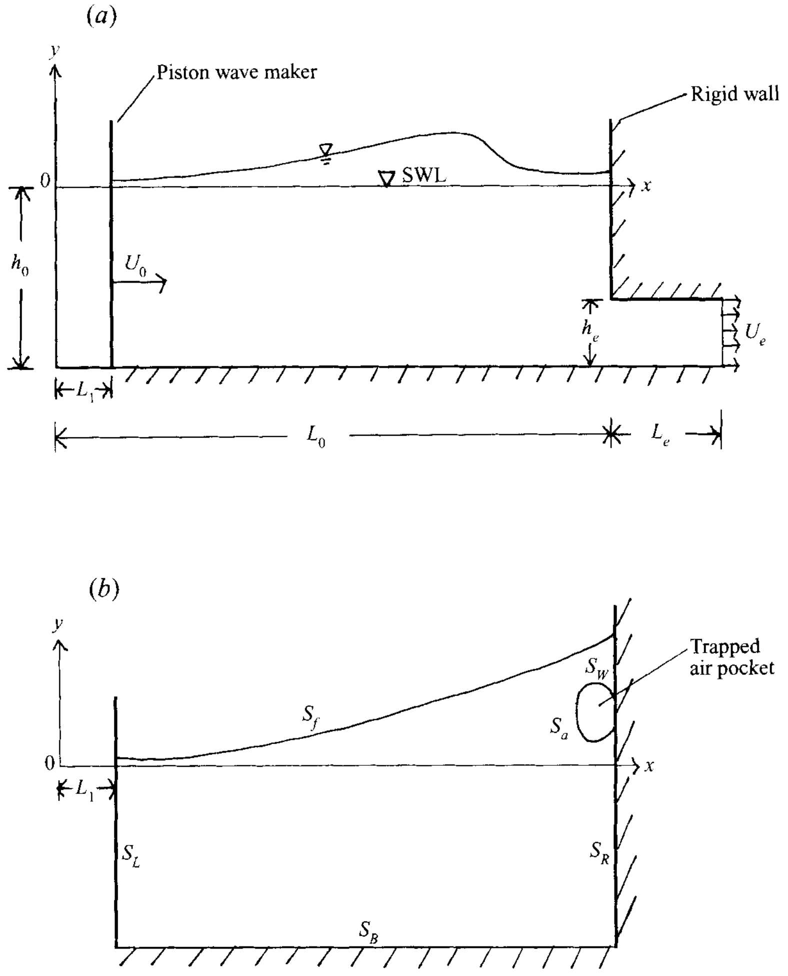

FIGURE 1. Definition sketches for a plunging wave impact on a vertical wall in a numerical tank for (*a*) before impact; and (*b*) after impact.

different locations on the wall. Different breaking wave profiles and kinematics are obtained by numerical testing and adjusting the parameters L_0, L_1, U_0 and h_e. For all of the cases selected (see Appendix B), a plunging breaker is formed which impacts S_R in the form of an oblique wedge (see figure 5). After impact (see figure 1*b*), this plunger tip spreads out into a wetted area S_W on the wall, trapping an air pocket below between the interior free surface of the breaker, S_a, and the wall.

The mathematical formulation and the MEL numerical scheme used in stages (i) and (iii) follow the general approach of Vinje & Brevig (1981). Details of the implementation and refinements can be found in Dommermuth *et al.* (1988) and Tanizawa & Yue (1992). For completeness, a brief summary is given below.

The two-dimensional potential flow can be described by the complex velocity potential

$$\chi(z,t) = \phi(z,t) + \mathrm{i}\psi(z,t), \tag{2.1}$$

where $z = x + \mathrm{i}y$, $\mathrm{i} = \sqrt{-1}$, and ϕ and ψ are the velocity potential and stream function, respectively. Since χ is analytical in the fluid domain, Cauchy's integral theorem applies, from which an integral equation for χ is obtained (e.g. Carrier, Krook & Pearson 1966):

$$\alpha i \chi(z_0, t) = \int_C \frac{\chi(z,t)}{z - z_0} \mathrm{d}z, \tag{2.2}$$

where the boundary of the fluid domain is $C = S_L \cup S_B \cup S_R \cup S_f$ for $t < t_I$ (figure 1*a*), and $C = S_L \cup S_B \cup S_R \cup S_a \cup S_W \cup S_f$ for $t > t_I$ (figure 1*b*), and $z_0 \in C$. In (2.2), the Cauchy principal value of the integral is implied, and α is the interior angle at z_0. Taking real and imaginary parts of (2.2), second-kind Fredholm integral equations are obtained respectively for ϕ on $S_L \cup S_B \cup S_R$ and ψ on $S_a \cup S_f$.

The boundary conditions on C are given from the problem specification. For simplicity, only the conditions for $t > t_I$ (figure 1*b*) are given here (similar conditions apply for $t < t_I$). The normal velocity on the wave maker is specified as

$$\psi = \begin{cases} U_0(y+1) & \text{for} \quad t < L_1/U_0 \\ 0 & \text{for} \quad t \geqslant L_1/U_0 \end{cases} \tag{2.3}$$

on S_L. There is no flux through the bottom and the right-hand wall:

$$\psi = \begin{cases} 0 & \text{on} \quad S_B \cup S_R \\ c(t) & \text{on} \quad S_W \end{cases} \tag{2.4}$$

where $c(t)$ is a function of time to be determined by solving the boundary-value problem.

On the free surface, the kinematic boundary condition reads

$$\frac{\mathrm{D}z}{\mathrm{D}t} = \frac{\partial \chi^*}{\partial z} \quad \text{on} \quad S_f \cup S_a, \tag{2.5}$$

and the dynamic boundary condition is given by Bernoulli's equation

$$\frac{\mathrm{D}\phi}{\mathrm{D}t} = \frac{1}{2}\left|\frac{\partial \chi}{\partial z}\right|^2 - y - (P - P_0) \quad \text{on} \quad S_f \cup S_a, \tag{2.6}$$

where $\mathrm{D}/\mathrm{D}t$ is the material derivative, $(\ )^*$ denotes complex conjugate, and P is equal to the atmospheric pressure P_0 on S_f, and equals the trapped air pressure $P_a(t)$ on S_a.

Assuming an adiabatic process in the air pocket, P_a is modelled using a polytropic gas law (e.g. Cole 1948):

$$\frac{P_a(t)}{P_0} = \left(\frac{V_0}{V_a(t)}\right)^{\gamma_a} \tag{2.7}$$

where $V_a(t)$ is the instantaneous volume (area) of the air pocket, V_0 its initial value at impact, and γ_a the polytropic gas constant. For air, γ_a=1.4 is used in the simulations, except in §6 where γ_a is adjusted to account for air leakage effects.

As in typical MEL simulations, the dynamical conditions (2.5) and (2.6) are integrated in time for z and ϕ on $S_f \cup S_a$ starting from initial conditions. A fourth-order Runge–Kutta scheme is used for the time integration with dynamic time-step sizes based on the surface velocity and spatial discretization (Dommermuth *et al.* 1988). A regridding scheme based on smoothing splines (Tanizawa & Yue 1992) is employed to remove high-wavenumber instabilities. At each time instant, the complex velocity potential χ is obtained by solving the boundary integral equation (2.2) and the velocity $\partial\chi/\partial z$ is calculated. To calculate the pressure on the wall from Bernoulli's equation, $\partial\phi/\partial t$ must be determined. To avoid finite differencing, a boundary-value problem for $\partial\chi/\partial t$ is solved using an equation similar to (2.2) but with χ replaced by

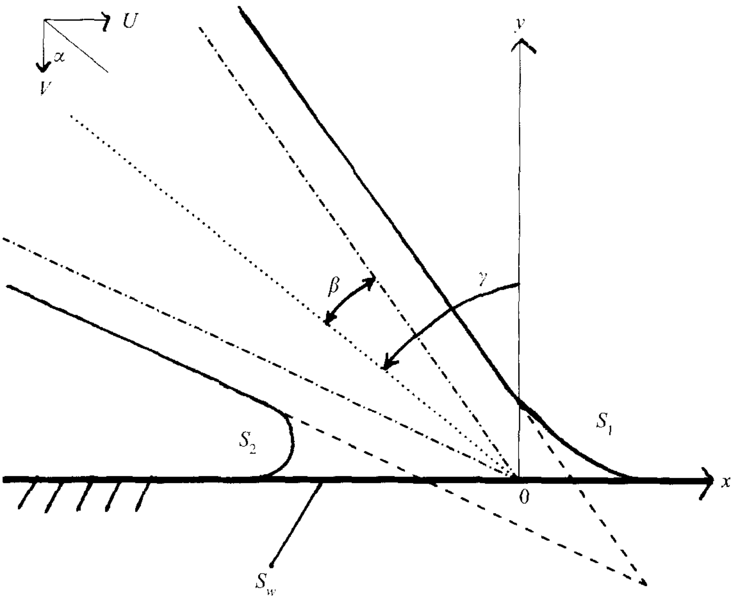

FIGURE 2. Definition sketch of a liquid wedge obliquely impinging on a rigid wall at the instant of impact (— · — ·); shortly after impact (——) (the matched similarity profile); and the profile in the absence of the wall (- - - -).

$\partial\chi/\partial t$. The corresponding boundary conditions for $\partial\phi/\partial t$ on $S_f \cup S_a$ and $\partial\psi/\partial t$ on $S_L \cup S_R \cup S_B \cup S_w$ are obtained from the corresponding expressions for ϕ and ψ given by (2.6) and (2.3), (2.4) respectively.

3. Modelling the initial stage of impact

The initial stage of impact starts as the tip of the plunging breaker touches the wall at $t = t_I$. After this, the generally converging jet tip undergoes a rapid transition to a diverging jet or 'splash' on the wall (see figure 5). During this short period, $t_I \leqslant t \leqslant t_I + \Delta t_I$, the effect of the trapped air represented by its volume change is negligible, and a local solution can be obtained by modelling the jet tip as a liquid wedge moving with uniform constant velocity towards the plane wall. For a symmetric normal impact, the problem has been considered by Borisova *et al.* (1959) and Cumberbatch (1960). In the following (also in Appendix A), the method of Borisova *et al.* (1959) is extended to the more general case of non-symmetric oblique impact of a liquid wedge.

3.1. *Approach*

Referring to figure 2, a coordinate system (x, y) is chosen with a plane rigid wall located at $y = 0$. A liquid wedge, assumed to extend to $y \to \infty$ moves with a uniform velocity $(U, -V)$ towards the wall. Initially, at $t = 0$, the tip of the wedge is in contact with the wall at $(0, 0)$. The geometry of the wedge is defined by its semi-angle β and its inclination γ measured from the y-axis to the bisector of the wedge.

For $t > 0$, the wedge spreads out along the wall as shown in figure 2 (solid line). The fluid domain D is bounded by the wetted area S_W on the wall, the wedge edges S_1 and S_2, and S_∞ at infinity. The velocity potential $\phi(x, y, t)$ for the flow is governed

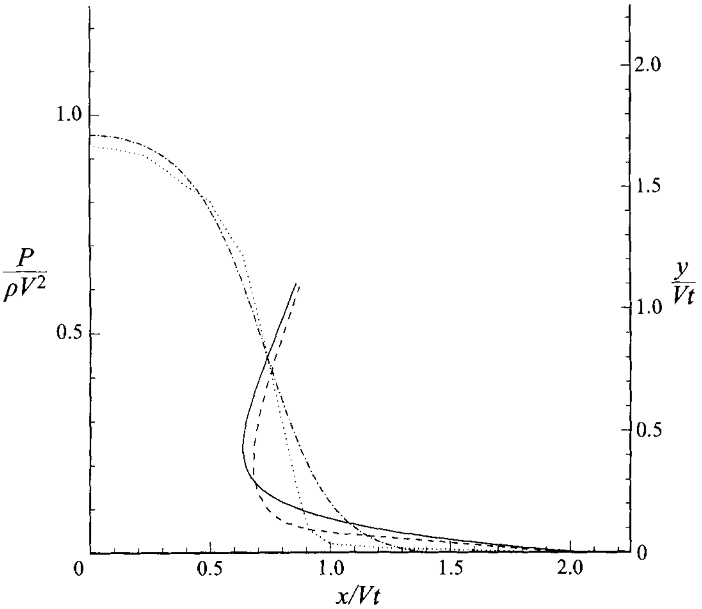

FIGURE 3. Comparison between the present similarity solution with that of Cumberbatch (1960) for the normal impact of a $\beta = 22.2°$ semi-angle wedge on a wall. Pressures (left-hand axis): present result (— · — ·) and Cumberbatch (1960) (· · · ·). Free-surface profiles (right-hand axis): present result (——) and Cumberbatch (1960) (— — —).

by

$$\nabla^2\phi(x,y,t) = 0 \quad \text{in} \quad D\,, \tag{3.1}$$

$$\frac{\partial\phi}{\partial y} = 0 \quad \text{on} \quad y = 0\,, \tag{3.2}$$

and

$$\nabla\phi = U\boldsymbol{i} - V\boldsymbol{j} \quad \text{at} \quad S_\infty. \tag{3.3}$$

The free surfaces on the two sides of the wedge S_i are defined by $x = S_i(y,t)$, $i = 1, 2$, $S_1 > S_2$. On S_i, ϕ satisfies nonlinear kinematic and dynamic boundary conditions

$$\frac{\partial\phi}{\partial x} = \frac{\partial S_i}{\partial t} + \frac{\partial\phi}{\partial y}\frac{\partial S_i}{\partial y} \quad \text{on} \quad x = S_i(y,t)\,, \tag{3.4}$$

$$\frac{\partial\phi}{\partial t} + \frac{1}{2}\left[\left(\frac{\partial\phi}{\partial x}\right)^2 + \left(\frac{\partial\phi}{\partial y}\right)^2\right] = 0 \quad \text{on} \quad x = S_i(y,t)\,; \tag{3.5}$$

$i = 1, 2$, and the Bernoulli constant is absorbed into ϕ in (3.5).

The initial-boundary-value problem for the non-symmetric normal ($U = 0$) impact problem is solved in terms of a similarity solution (see Appendix A for details). The more general oblique impact case represented by (3.3) can be obtained by superimposing a uniform horizontal velocity U on the flow.

3.2. *The results of the similarity solution*

As a first check, the case of symmetric normal impact of a wedge is considered. Figure 3 shows the present solution for the case $\beta = 22.2°$ compared to that of Cumberbatch (1960). The results for both the surface profiles and pressure distribution

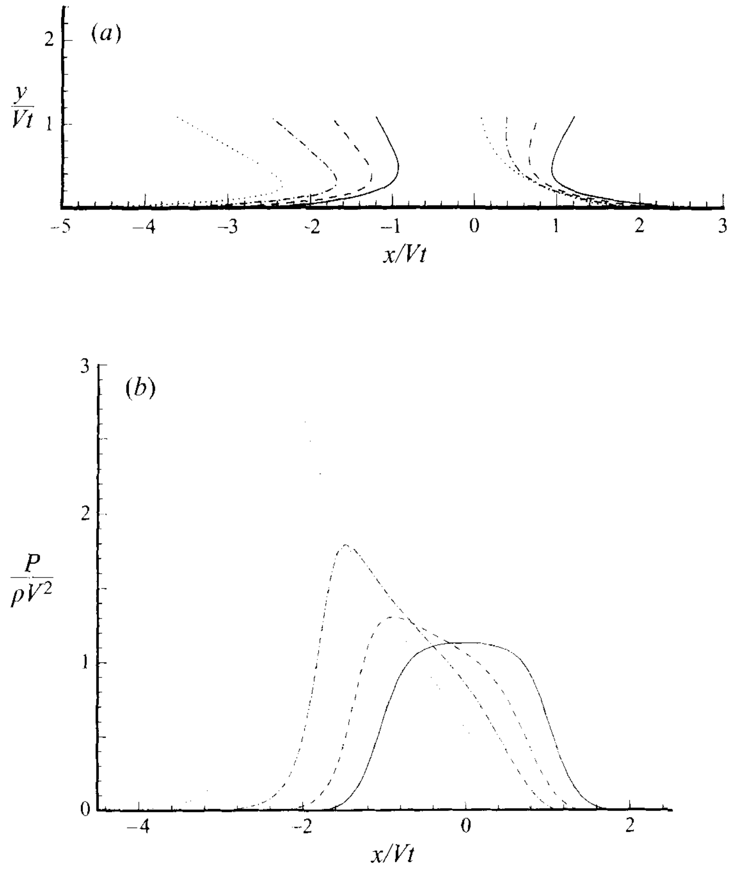

FIGURE 4. Free-surface profiles (*a*), and wall pressures (*b*), for a wedge impact with $\beta = 30°$ and $\gamma = 0°$ (——); 10° (– – –); 20° (— · — ·); and 30° (· · · ·).

on the wall are satisfactory. The difference between the present results and those of Cumberbatch (1960) stems from the different assumptions on the free-surface profiles close to the wall: in the present approach, an exponential function is assumed, while in Cumberbatch (1960), a linear function is used.

The non-symmetric case is new. Figure 4 shows the surface profiles and wall pressures for the case of normal impact with $\beta = 30°$ and a range of inclination angles γ. As γ increases, the thickness of the S_1 spray root also increases. For the same V, it is evident that the fluid area that would pass $y = 0$ in the absence of the wall increases with $|\gamma|$. In the presence of the wall, one argues physically that more of the fluid momentum is displaced by the wall for $\gamma > 0$. This can be seen from figure 4(*b*), where the maximum wall pressure is greater for $\gamma > 0$, accompanied by a shift of the location of the maxima to the left as γ increases.

Some researchers (Whillock 1987; Kirkgöz 1991) have reported the effect on the maximum wall impact pressure due to a change of the inclination angle of the wall relative to an approaching breaker. They find that the measured maximum impact pressures are greater for certain wall inclination angles than for a vertical wall. It is clear that the maximum impact pressure is not only a function of relative position between the breaker and the wall at the instant of the impact, but also depends

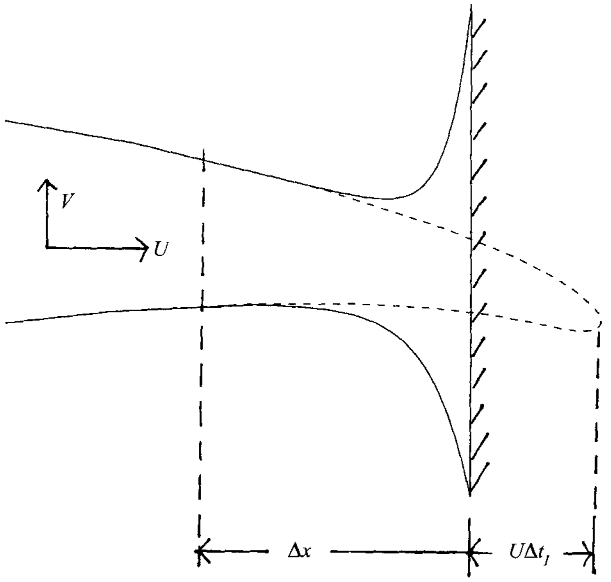

FIGURE 5. Schematic showing matching of profiles of the similarity solution (——) and the numerical solution (in the absence of the wall) (— — —) a short time Δt_I after the impact.

on the local plunger–wall geometry. More results of the wedge impact problem are presented and discussed in §5.

4. Numerical simulations

The MEL simulations for the plunging wave impact on a vertical wall are carried out starting from rest ($t = 0$) until the time of impact at $t = t_I$. The simulations are then continued again with a trapped air pocket from the similarity solution of §3 a short time Δt_I afterwards, i.e. for $t > t_I + \Delta t_I$.

4.1. *Matching to the similarity solution*

The oblique impact of the wedge in §3 depends on the parameters $(U, -V)$, β, and γ. These quantities for a specific plunging wave are obtained from the MEL simulation of the problem. The matching procedure is illustrated in figure 5. The numerical simulation is allowed to continue a short time longer to $t = t_I + \Delta t_I$ *assuming* that the wall is absent. This numerical solution at a small horizontal distance Δx from the wall is then matched to the similarity solution at $t = t_I + \Delta t_I$. With the geometric parameters of the wedge in the similarity solution taken from the numerical simulation, the matching of the surface profiles is generally quite smooth. The numerical and similarity solutions for the velocity potential ϕ in general differ by a constant, although the velocity is smooth. The solution is simply to integrate the complex velocity $\partial\chi/\partial z$ along the free surface with the values of ϕ and ψ specified at the matching points. This yields a smooth distribution in ϕ and ψ along the matched free surfaces. In practice, with a suitable choice of Δx (given Δt_I), the MEL simulation of the matched solution beyond $t_I + \Delta t_I$ continues smoothly, and numerical smoothing of the profile or potential, while available, is generally not required. Evidence of numerical convergence of the final solution (say in the maximum wall pressure) is presented in the next subsection.

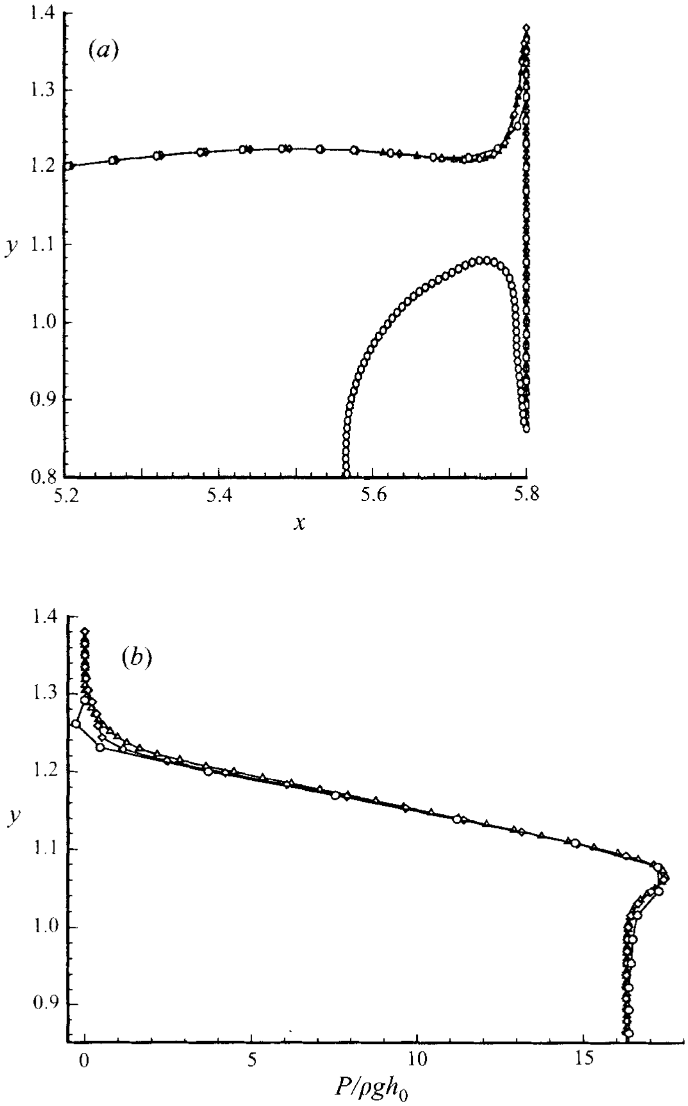

FIGURE 6. Free-surface profiles of the spreading jet (*a*), and wall pressures (*b*) for different panel lengths for Case 6 (Appendix B) with $P_0/\rho U^2 = 5$ at $t = t_l + 0.047$. The minimum panel lengths on the free surface and on the wall are respectively, 0.01 and 0.0075 (△), 0.02 and 0.015 (◇), and 0.04 and 0.03 (○).

4.2. *Convergence studies*

To validate the overall simulation scheme, systematic convergence tests are performed for varying panel (segment) sizes, integration time steps, and matching parameters Δt_l and Δx. Figure 6 shows a representative case (Case 6 in Appendix B) for the free surface and wall pressure profiles near the impact zone for decreasing panel sizes. The convergence as the panel sizes are reduced is evident. Results for the maximum pressure on the wall also converge and are stable when the size of the time step is reduced.

Convergence with respect to the matching parameters is also verified. For example, when the simulation corresponding to Case 6 is performed using two different sets of $(\Delta t_l, \Delta x)$ corresponding to (0.013, 0.03) and (0.018, 0.04), the difference in the maximum impact pressures between the two calculations is found to be about 5%, while that in the rise time is about 2%.

Based on the convergence studies, the parameters for all the simulations in this study are chosen as follows. Non-equal panel lengths are used for the exterior free surface, S_f, with maximum and minimum panel lengths 0.25 and 0.0025, respectively; 100 panels of equal panel lengths are used for the interior surface S_a; and the (constant) panel length on the wetted area of the impact zone, S_W, is 0.0075. As the spray roots develop and spread out along the wall, they eventually become extremely thin. To permit the simulation to continue, a procedure similar to Zhao & Faltinsen (1993) is adopted wherein the tips are truncated and matched to uniform jets. In this case, the minimum thickness of the spreading jet is set to be 0.0025. For the Runge–Kutta time integration, the dynamic time-step sizes are set to be equal to $0.05L_{min}/V_{max}$, where L_{min} is the smallest panel length on S_f, and V_{max} the maximum velocity on S_f. The matching parameter values are chosen with $\Delta t_I \approx 0.013$ and $\Delta x \approx 0.03$ for the twelve cases in Appendix B. Using these simulation parameters, subsequent numerical results for the surface profiles and wall pressure (maximum value and rise time) are expected to have converged to within $O(5\%)$.

4.3. *The results of the numerical simulation*

The main dynamical quantities of interest in this study are the maximum wall pressure P_m (see definition in §5.1) and the rise time T_r for P_m to obtain after initial impact. To understand the dependence of P_m and T_r on the kinematic and geometric parameters of the problem, a set of twelve different impact configurations is generated and a number of simulations for different initial air pocket pressures P_0 are carried out for each of the twelve configurations. The kinematic and geometric particulars of the twelve initial impact configurations are given in Appendix B.

To illustrate the general features of the plunging wave impact, we present in the following Case 6 (see Appendix B) with $P_0/\rho U^2 = 5$ as a representative case. Figure 7 shows the free surface and wall pressure profiles at several time instants beyond the initial impact. Following the initial impact, the plunging wave forms a diverging jet along the wall trapping an air pocket below. As the surrounding fluid advances towards the wall, the air pocket is compressed. At $t - t_I \approx 0.06$, the volume of the air pocket $V_a(t)$ reaches a minimum value, while the air pocket pressure $P_a(t)$ attains a maximum according to the polytropic law (2.7). The pressure change inside the air pocket directly affects the pressure distribution on the wall as shown in figure 7(*b*). As the air is compressed by the fluid, the pressure gradient in the fluid changes rapidly. When $P_a(t)$ reaches a maximum, the pressure on the wetted wall adjacent to the air pocket also becomes maximum and is generally greater than but close to the maximum P_a value. Thus both the maximum wall pressure P_m and rise time T_r are directly related to the effect of the trapped air.

The evolution of the trapped air pocket pressure $P_a(t)$ and volume $V_a(t)$ relative to initial values are plotted in figure 8. As $V_a(t)$ decreases and then increases, the potential energy of the trapped air changes accordingly. Figure 9(*a*) shows the changes in the air potential energy and the fluid potential and kinetic energies during this phase. For this case, the maximum potential energy stored in the air pocket can be as much as 15% of the total fluid energy at impact. Note that during this relatively short phase, the rise of the pocket is primarily due to the vertical pressure gradient associated with the hydrodynamic pressure, not the gravity. Thus, the change in the potential energy of the fluid is negligible, and the air pocket effectively 'cushions' the kinematic energy of the impinging fluid.

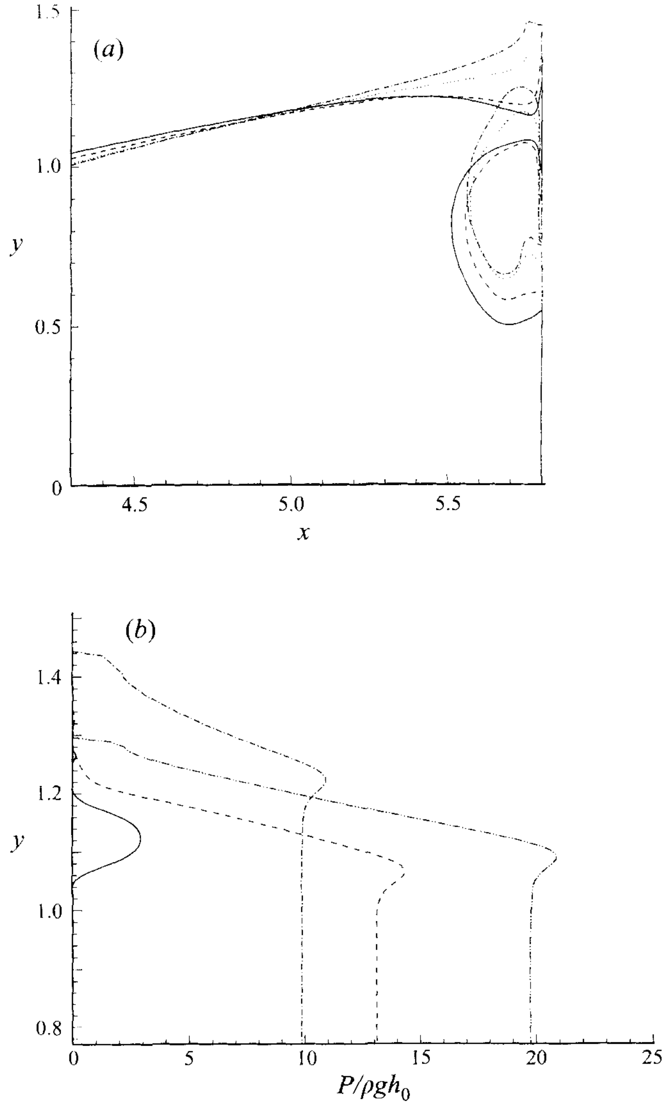

FIGURE 7. Temporal evolution of (*a*) surface profile and (*b*) pressure distribution on the wetted wall for plunging wave impact Case 6 (Appendix B) with $P_0/\rho U^2 = 5$; at $t - t_I = 0.0125$ (——), 0.0406 (- - - -), 0.0606 (— · · —), 0.0762 (· · · ·), 0.0902 (— · — ·).

The corresponding results for the horizontal momentum of the fluid and the total (force) impulse on the wall are given in figure 9(*b*), which shows the conservation of the total momentum. As the air is compressed to a minimum volume, the portion of the initial horizontal fluid momentum converted to force impulse on the wall is about 25%, of which 24% is associated with the force impulse on the wetted impact zone S_W.

Referring back to figure 7(*a*), it is seen that as P_a increases (above P_0), the upper limb of the fluid, which has the least inertia, is pushed upwards. In many real cases, this part of the fluid may be 'blown off' in the initial compression phase, or after a number of rising oscillations (see figures 17, 18, for example), after which the air pocket eventually aerates.

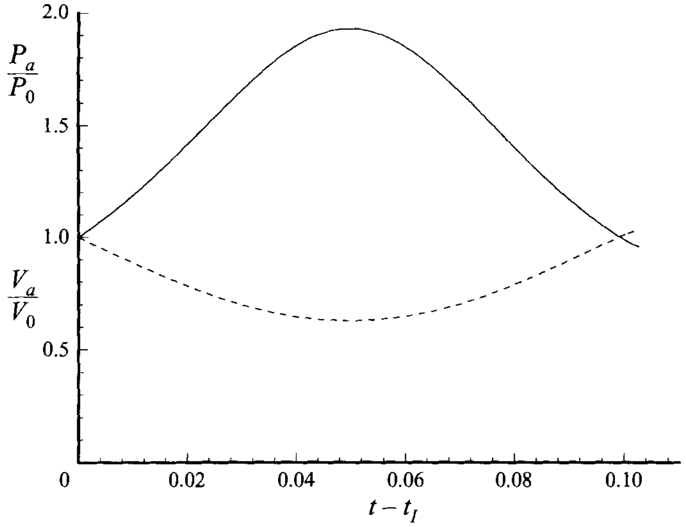

FIGURE 8. Temporal evolution of trapped air pressure (——), and volume (— — —) after impact for Case 6 (Appendix B) with $P_0/\rho U^2 = 5$.

5. Scaling law

The generation of a plunging breaker up to the point of impact is generally governed by Froude scaling. For the impact process itself, however, a different set of scaling laws must be sought due to the different time scales and physical mechanisms such as trapped air that are involved. Existing scaling laws for the impact process are generally obtained by extrapolating experimental or computational results without consideration of the many physical parameters involved. As a result, their utility tends to be limited (see the summary in Stive 1984; Blackmore & Hewson 1984). In this section, the controlling physical parameters and scaling laws for the maximum wall impact pressure P_m and the rise time of this maximum pressure T_r are sought for the present case of plunging wave impact on a rigid vertical wall involving a trapped air pocket.

5.1. *Dimensional analysis and flow regimes*

The maximum wall impact pressure (excess over atmospheric value P_0) is defined as $P_m \equiv \max_{y,t} P(y,t) - P_0$, $y \in S_w \cup S_R$; while the pressure rise time is defined to be $T_r \equiv t_m - t_I$, where t_m is the instant when P_m is reached. Our interest here is to relate P_m and T_r to the local parameters of the impact problem with the assumption that, for similar local conditions, the scaling should be similar regardless of the details of the original generation mechanisms.

In addition to P_0, the following local parameters at the instant of impact are identified (refer to figure 10*a*): the (horizontal) velocity of the plunger tip U; and the lengths h, H and ℓ associated with the plunging wave and air pocket geometry. It is convenient to define an equivalent dimension of the air pocket, $L \equiv (H\ell)^{1/2}$. Using this definition, the problem relates the dimensionless parameters $P_m/\rho U^2$, $T_r U/L$, $P_0/\rho U^2$, gL/U^2, and G_i, where G_i are dimensionless geometric parameters such as h/L, H/L and ℓ/L. Noting that the time scale associated with the air pocket oscillation, $L(\rho/P_0)^{1/2}$, is generally much smaller than that associated with gravity, $(L/g)^{1/2}$, (for $L < O(10)$ m, say), the effect of gravity can generally be neglected during the impact

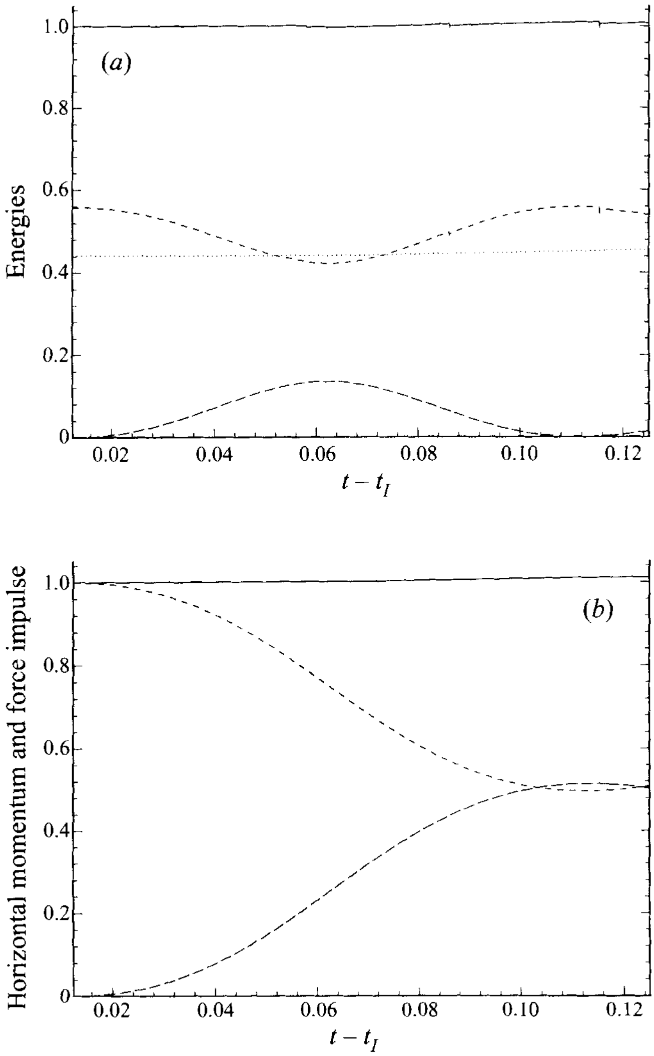

FIGURE 9. Temporal evolution of (*a*) energy and (*b*) momentum after impact for Case 6 (Appendix B) with $P_0/\rho U^2 = 5$. For (*a*): fluid kinetic energy (- - - -); fluid potential energy (· · · ·); trapped air potential energy (— — —); and total mechanical energy (——). For (*b*): horizontal fluid momentum (- - - -); wall force impulse (— — —); and the sum of the two (——).

phase. Thus, $P_m/\rho U^2$ and $T_r U/L$ can be represented in the following functional forms

$$\frac{P_m}{\rho U^2} = f_P \left(\frac{P_0}{\rho U^2}, G_i \right), \tag{5.1}$$

$$T_r \frac{U}{L} = f_T \left(\frac{P_0}{\rho U^2}, G_i \right). \tag{5.2}$$

Ignoring the geometric variations G_i for the time being, three parameter regimes can be identified depending on the dynamical parameter $P_0/\rho U^2$.

Regime I is characterized by $P_0/\rho U^2 \ll 1$, wherein the inertia of the fluid dominates that of the air, and the dynamics of the latter can be ignored despite substantial compression of the air pocket. In this regime, $P_m/\rho U^2$ is primarily a function of the

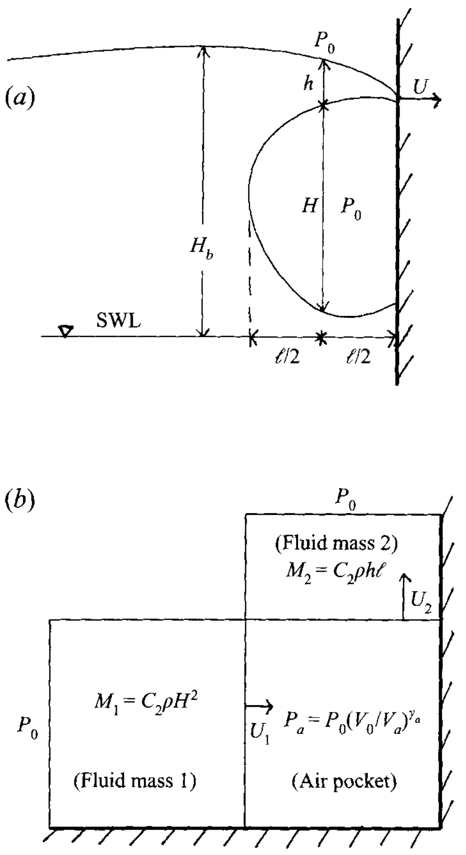

FIGURE 10. (*a*) Schematic of the plunger tip at the instant of impact showing: h, the depth of the plunger tip; H, the height of the air pocket; H_b, the height of the plunger measured from the plunger crest to the still-water level; ℓ, the width of the air pocket; U, the horizontal impact velocity; and P_0, the (initial) trapped air pressure. (*b*) The corresponding two-mass piston model with the effective fluid masses M_1 and M_2.

plunging jet geometry alone, i.e.

$$\frac{P_m}{\rho U^2} = f_P(G_i). \tag{5.3}$$

Regime II covers the moderate range of $P_0/\rho U^2$ wherein both the effects of the fluid and the trapped air are important and (5.1) and (5.2) apply. Regime III corresponds to $P_0/\rho U^2 \gg 1$, for which the excess pressure due to impact is small relative to P_0. In what follows, only regimes I and II are further considered.

5.2. *Regime I: wedge impact approximation*

For $P_0/\rho U^2 \ll 1$, the maximum wall pressure may be approximated by that due to the wedge impact of §3, and G_i are simply the wedge angles β and γ:

$$\frac{P_m}{\rho U^2} = f_P(\beta, \gamma). \tag{5.4}$$

This relationship is illustrated in figure 11(*a*), in which $P_m/\rho U^2$ is plotted as a function of wedge semi-angle β for a range of inclination angle γ. The figure highlights the strong dependence of $P_m/\rho U^2$ on γ, especially for moderate to large β. As discussed

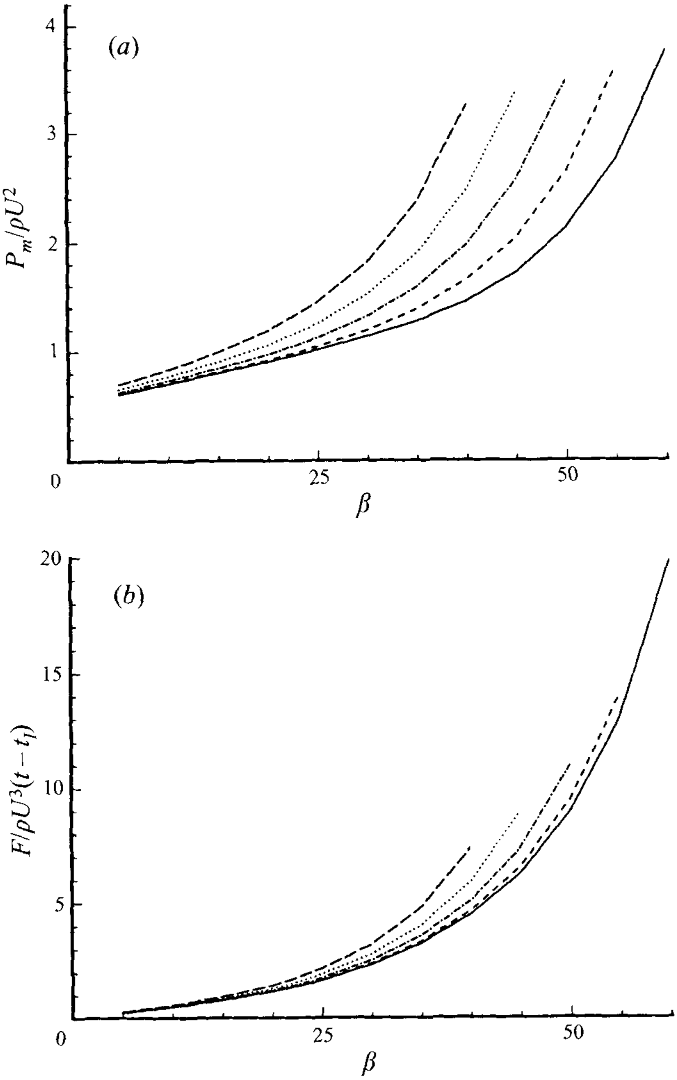

FIGURE 11. Maximum impact pressures (*a*), and total impact forces (*b*) as a function of semi-wedge angle β and inclination angle $\gamma = 0°$ (——); 5° (- - - -); 10° (— · — ·); 15° (· · · ·); and 20° (— — —).

in §3.2, for a given U, the rate of fluid momentum transfer to the wall increases with γ, resulting in a larger impact pressure. As $\beta \to 0$, P_m converges to the stagnation pressure $\rho U^2/2$. Similar trends are seen in the impact force F on the wall as shown in figure 11(*b*), except now $F \to 0$ as $\beta \to 0$.

5.3. *Regime II: modified Bagnold model*

In this regime of moderate $P_0/\rho U^2 = O(1)$, f_P and f_T depend on more than one parameter and one would in principle need to examine the combined parameter space ($P_0/\rho U^2$, G_i) systematically to determine (5.1) and (5.2). An attractive alternative is to obtain a simple physical model to represent the dependencies. Following Bagnold (1939) and extending it to include more geometric information, a simple dynamical system, illustrated in figure 10(*b*) is constructed . The dynamical system consists of two fluid masses: $M_1 = C_1\rho H^2$ and $M_2 = C_2\rho h\ell$, corresponding to the fluid volume behind and above the air pocket respectively. Here, C_1 and C_2 are empirical constants yet to be determined. These two masses act on an air piston which serves as a spring (see figure 10*b*). The initial velocities of M_1 and M_2 are specified as $U_1(0) = C_3U$ and $U_2(0) = 0$, respectively, where C_3 is another constant. The equations of motion for the two masses are

$$M_1\ddot{x}_1 = (P_a - P_0)H, \tag{5.5}$$

$$M_2\ddot{x}_2 = (P_a - P_0)\ell. \tag{5.6}$$

For $P_a = P_0(V_0/V_a)^{\gamma_a}$ and relative displacement $X = (x_1/\ell + x_2/H) < 1$, (5.5) and (5.6) reduce to a single equation for X:

$$\left(\frac{H\ell M_1M_2}{\ell^2M_1 + H^2M_2}\right)\ddot{X} + \gamma_aP_0X = O(X^2). \tag{5.7}$$

To the leading-order approximation in X, the frequency of the (linear) system above is

$$\omega^2 = \gamma_aP_0\left(\frac{H}{\ell M_1} + \frac{\ell}{HM_2}\right). \tag{5.8}$$

Substituting in the expressions for M_1 and M_2 yields

$$\frac{\pi^2\rho H\ell}{4T_r^2\gamma_aP_0} = \frac{1}{C_1} + \frac{\ell}{hC_2}, \tag{5.9}$$

where $T_r = \pi/2\omega$. The maximum pressure P_m corresponding to the linear system is

$$\frac{P_m}{(\rho U^2\gamma_aP_0)^{1/2}}\left(\frac{\ell}{H}\right)^{1/2}\left(\frac{1}{C_1} + \frac{\ell}{hC_2}\right)^{1/2} = C_3. \tag{5.10}$$

From (5.9) and (5.10), we finally obtain

$$T_r\frac{U}{(H\ell)^{1/2}} = C_T\left(\frac{P_0}{\rho U^2}\right)^{-1/2}, \tag{5.11}$$

$$\frac{P_m}{\rho U^2} = C_P\left(\frac{P_0}{\rho U^2}\right)^{1/2}, \tag{5.12}$$

where C_P and C_T are now the undetermined empirical coefficients and are related to the geometric parameters (and C_1, C_2, C_3) by

$$C_T = \frac{\pi}{2}\left(\frac{hC_1C_2}{\gamma_a(\ell C_1 + hC_2)}\right)^{1/2}, \tag{5.13}$$

$$C_P = C_3\left(\frac{\gamma_aHhC_1C_2}{\ell(\ell C_1 + hC_2)}\right)^{1/2}. \tag{5.14}$$

5.4. *Estimation of C_P and C_T*

Equation (5.14) shows that C_P is a function of ℓ/H and ℓ/h. Of the two, ℓ/h is more important than ℓ/H since in the two-mass piston model (5.7), the frequency of the system is controlled by the body with the smaller mass.

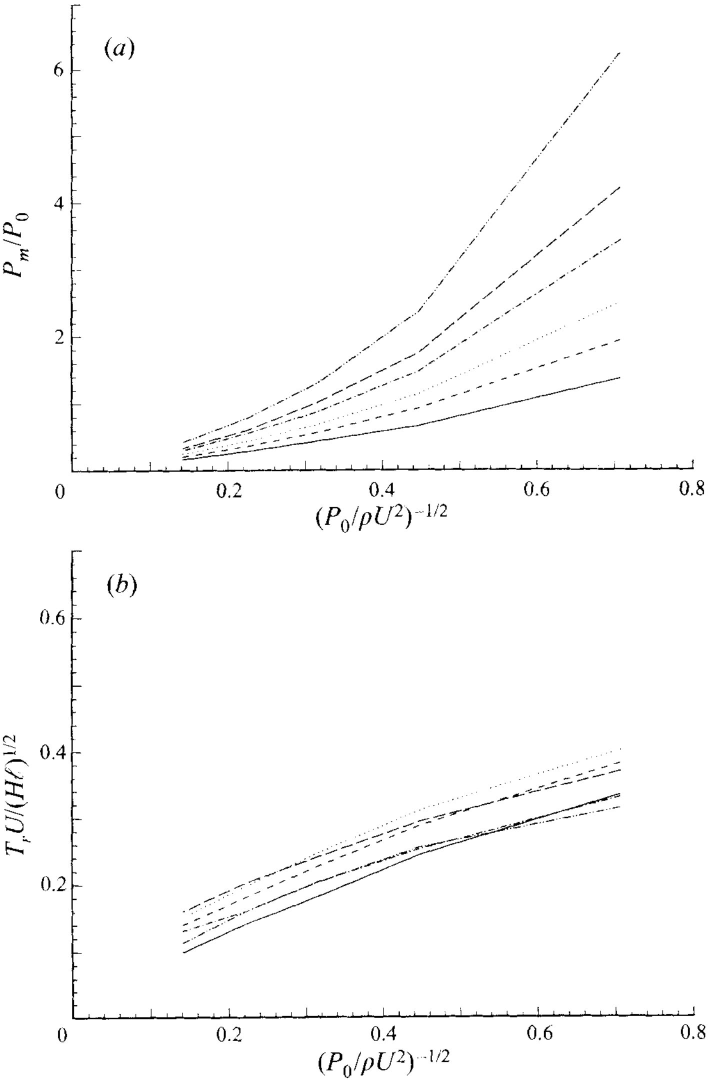

FIGURE 12. Normalized maximum pressure P_m/P_0 (*a*), and pressure rise time T_rU/L (*b*), as a function of $(P_0/\rho U^2)^{-1/2}$, from numerical simulations, for $\ell/h = 1.3$ (— · · · —); 1.9 (— — —); 2.1 (— · — ·); 2.4 (· · · ·); 3.3 (- - - -); and 4.9 (——).

To explore the dependence of C_P and C_T on ℓ/h and ℓ/H, numerical simulations are performed for the twelve (initial) plunger geometries in Appendix B, and in each case, for a range of $P_0/\rho U^2 = 2$, 5, 10, 20 and 50 – a total of sixty simulations.

Representative results from these simulations are plotted in figure 12 for P_m/P_0 and T_rU/L versus $(\rho U^2/P_0)^{1/2}$ for the range of ℓ/h represented in Appendix B. The values of C_P in (5.12) calculated from all (sixty) simulation cases are plotted in figure 13 as a function of ℓ/h. It is apparent that C_P is roughly inversely proportional to ℓ/h for a given $P_0/\rho U^2$. Physically, as h increases, the effective fluid mass above the air pocket increases, resulting in a greater P_m as well as the duration of the compression T_r. Alternatively, for a given compression of the air pocket in the horizontal direction, a smaller ℓ corresponds to a larger volume change of the pocket, so a larger P_m is

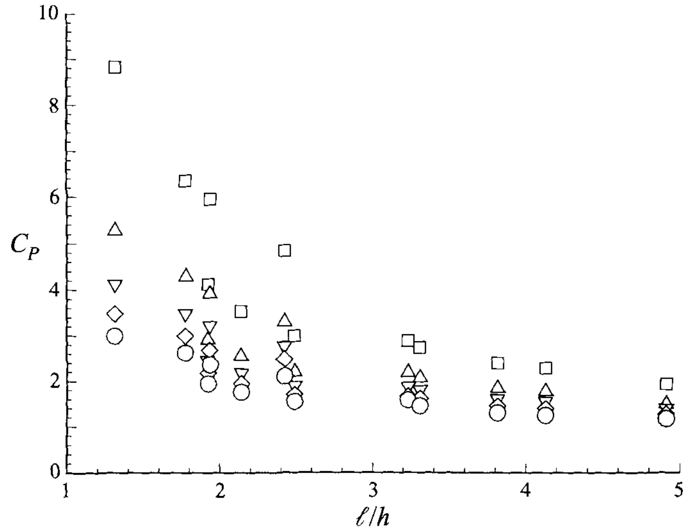

FIGURE 13. Distributions of C_P as the function of ℓ/h, from numerical simulations, for $P_0/\rho U^2 = 2$ (□), 5(△), 10(▽), 20(◇) and 50(○).

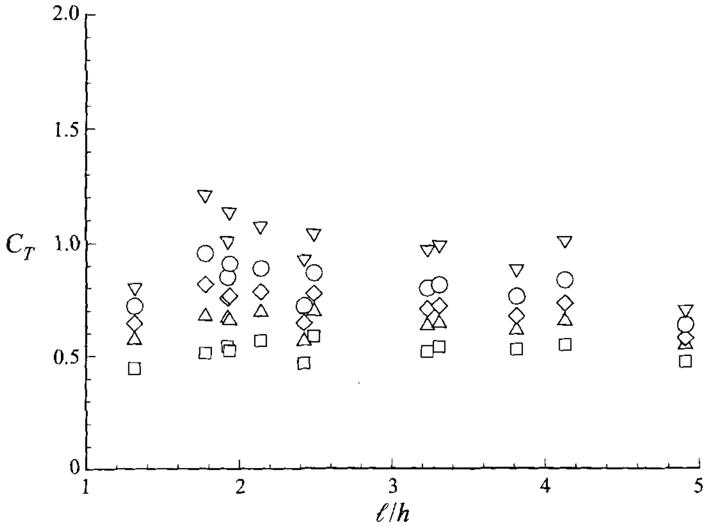

FIGURE 14. Distributions of C_T as function of ℓ/h, from numerical simulations, for $P_0/\rho U^2 = 2$ (□), 5(△), 10(▽), 20(◇) and 50(○).

produced. This finding is consistent with the experimental observations of Hattori *et al.* (1994). As was suggested earlier, no strong dependence of C_P on ℓ/H is found for the same cases computed. Evidently, since the fluid strikes the air pocket almost horizontally, the change in the air pocket dimension occurs mainly in its width ℓ, so that a different pocket depth H does not strongly affect the ratio of the initial volume to the instantaneous volume of the trapped air.

Assuming that C_P depends on one geometric parameter ℓ/h, a χ^2 fitting (e.g. Press *et al.* 1989) is applied to the data in figure 13 to obtain that $C_P \simeq 5.9(l/h)^{-0.9}$, or when C_P is treated as a constant, a value of $C_P \simeq 2.6$. In a similar fashion, the C_T values from the simulations are plotted against ℓ/h in figure 14. The dependence on

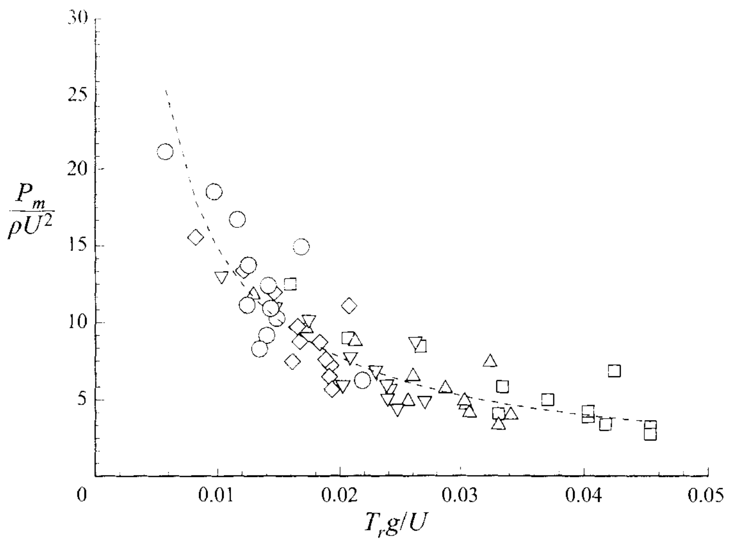

FIGURE 15. Correlation between $P_m/\rho U^2$ and $T_r g/U$, from numerical simulations, for $P_0/\rho U^2 = 2$ (□); 5 (△); 10 (▽); 20 (◇); and 50 (○). A χ^2 fit corresponding to $P_m/\rho U^2 \approx 0.2(T_r g/U)^{-0.95}$ (- - - -).

ℓ/h is weak over the range of ℓ/h between 1.3 and 5 represented by the data, and a constant value fit of the data yields $C_T \simeq 0.73$. In summary, the scaling laws based on the cases examined above can be expressed as

$$\frac{P_m}{\rho U^2} \simeq 2.6\left(\frac{P_0}{\rho U^2}\right)^{1/2}, \quad \text{or} \quad \frac{P_m}{\rho U^2} \simeq 5.9\left(\frac{h}{\ell}\right)^{0.9}\left(\frac{P_0}{\rho U^2}\right)^{1/2}, \tag{5.15}$$

$$T_r\frac{U}{(H\ell)^{1/2}} \simeq 0.73\left(\frac{P_0}{\rho U^2}\right)^{-1/2}. \tag{5.16}$$

The correlation between P_m and T_r can also be obtained from the simulation data and is presented in figure 15. A simplified relation without involving $P_0/\rho U^2$ and h/ℓ is obtained with χ^2 fit which gives $P_m/\rho U^2 \simeq 0.2(T_r g/U)^{-1}$. This relationship, $P_m \propto T_r^{-1}$, is in agreement with the measurements of Blackmore & Hewson (1984), Kirkgöz (1990), and Hattori *et al.* (1994). We mention, finally, that the present simulation datasets have also been examined for possible correlation between the maximum impact force and its rise time. The results, however, show appreciable scatter and no systematic dependence is identified.

6. Direct comparison with experiment

6.1. *Procedures*

To assess the validity and usefulness of the present simulations and scaling laws, a direct simulation of the experiment of Chan & Melville (1988, hereafter referred to as CM) is performed for the impact of a deep-water breaking wave against a vertical wall. The specific case considered corresponds to case '(*b*)' of CM (see figure 16). The numerical simulation duplicates exactly the experimental conditions in terms of the vertical wall location, $L_0 = 11.75$, and the paddle motion of the wave maker (cf. Dommermuth *et al.* 1988). In the experiments, the physical still water depth

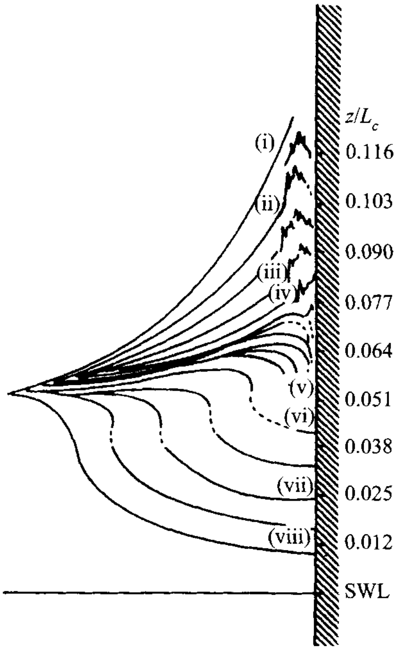

FIGURE 16. Surface profiles of the experiments of CM obtained from high-speed films at *ca.* 1100 frames per second. The time from the start of the wave maker in seconds for each profile is: (i) 17.014; (ii) 17.004; (iii) 16.984; (iv) 16.979; (v) 16.968; (vi) 16.964; (vii) 16.944; and (viii) 16.924. Elevations relative to still water level (SWL) are also indicated. The parameters of the experiment are: $h_0 = 0.6$ m, $L_0/h_0 = 11.755$, and characteristic incident wave period $T_c = 1.136$ s and wavelength $L_c = 1.936$ m. (Reproduced, with permission, from CM figure 6*b*.)

is $h_0 = 0.6$ m, and for comparison to the measurements, the density of water ρ, gravity g and atmospheric pressure P_0 are chosen simply as 10^3 kg/m^{-3}, 10 m/s^{-2} and 10^2 kN/m^{-2}, respectively. The numerical procedure used to generate the deep-water breaking wave up to the point of impact at the wall follows closely that of Dommermuth *et al.* (1988) with minor refinements on the regridding and smoothing procedures introduced by Taylor (1990).

6.2. *Free-surface profiles and velocities*

Figure 17 shows the computed free-surface profiles before and after impact at different time instants. These can be compared with the profiles obtained from experiments of CM in figure 16 (reproduced from CM figure 6*b*). Before impact, at $t - t_I \approx -0.053$, as the contact point on the wall ascends to about $y = 0.08$, the computed height of the plunger tip is 0.14. The corresponding value from the experiment (cf. profile (vii) in figure 16) is about 0.15 (the conversion factor from the experiment is $L_c/h_0 \simeq 3.23$). At the instant of impact, the height of the computed impact point is approximately 0.16, while from figure 16, this value is between 0.17 and 0.20. The time of impact is $t_I \simeq 51.18$ from the calculation, while the estimated value from CM is between 51.15 and 51.19 (these are converted from figure 16 after subtracting 4.44 s to account for a time delay of the wave maker in the calculation). As for the size of the air pocket at impact, an accurate reading from the experiment is difficult, although a qualitative estimate is still possible. From figure 16, if one measures the vertical distance between $z/L = 0.051$ and 0.064 and estimates the actual pocket dimension at the instant of impact to be approximately half that distance, one obtains a value of $H \approx \ell \approx 0.021$.

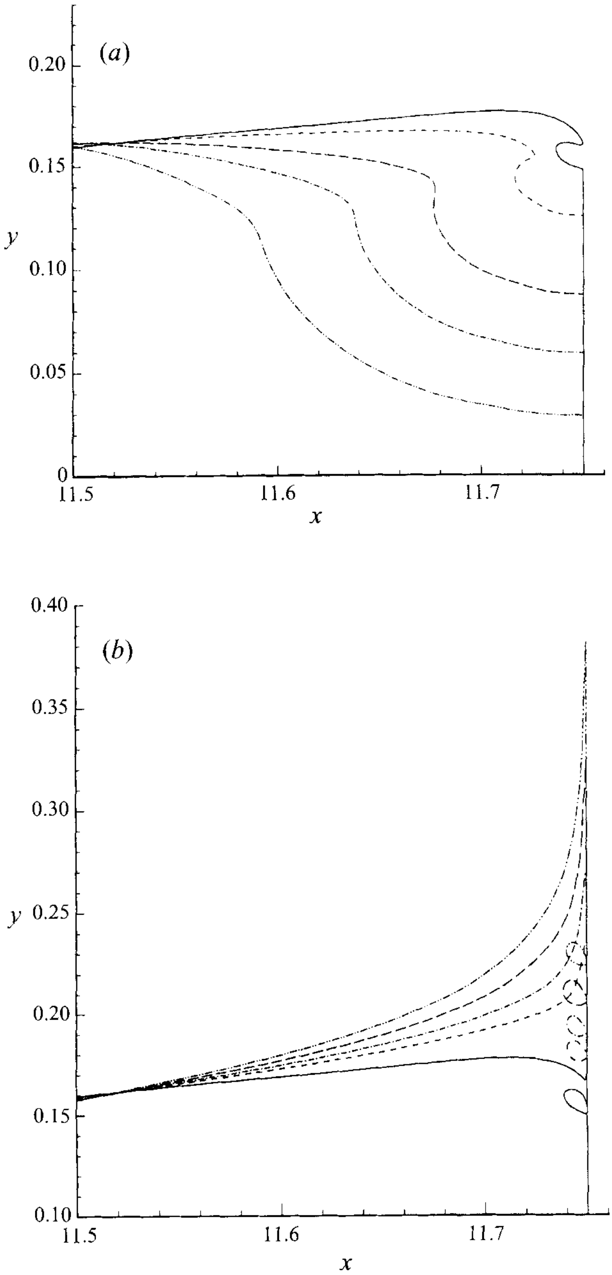

FIGURE 17. Free-surface profiles before impact (*a*) at $t-t_I = -0.134$ (— · · —); -0.072 (— · — ·); -0.053 (— — —); -0.017 (- - - -); -0.001 (——); and during impact (*b*) at $t-t_I = 0$ (——); 0.017 (- - - -); 0.026 (— · — ·); 0.039 (— — —); 0.054 (— · · —).

This is to be compared with calculated values of $H = 0.016$ and $\ell = 0.013$. The qualitative agreement is still reasonable.

In CM, the maximum horizontal crest speed of the breaking wave is measured in the absence of the vertical wall to be about 2 m s^{-2} ($U \simeq 0.82$), but no impact velocity at the instant of the impact is given. The numerical simulation shows a horizontal velocity of the plunger tip, U, increasing from $\sim$ 1.0 at an instant $t - t_I \simeq -0.07$ before impact to $\sim$ 1.37 at the instant of impact. The upward vertical tip velocity of the spreading jet on the wall just after impact at $y = 0.17$ and $t - t_I \simeq 0.0012$ is about 5.4. From figure 10(j) of CM, the vertical velocity of the jet tip at a similar stage is estimated to be about 4.9. Overall, the simulation of the impact wave profile and velocities agree with the experimental values to within about 10%.

6.3. *Wall pressure*

6.3.1. *Pressure oscillations*

CM observed that the oscillations in the measured wall impact pressures are associated with the trapped air. The measured frequency of the oscillations, which is inversely proportional to the volume of the trapped air pocket, ranges from 2 $\sim$ 5 kHz for high-frequency oscillations to 300 $\sim$ 800 Hz for low-frequency oscillations. Figure 18(a) plots the computed time history of the impact pressure (with $\gamma_a = 1.4$) at the location of the initial impact point of the plunger tip ($y = 0.16$). Also plotted is the relative volume change of the trapped air. The oscillation frequency here is about 500 Hz which is within the medium frequency range indicated by CM. Figure 18(a) also shows decay of the pressure oscillations with time. Figure 18(b) shows the time history of the impact force on the wall within the impact zone S_W. The impact force also exhibits the oscillating behaviour of the impact pressure. By examining the distribution of energy among the different components, it is found that the main energy exchange during the impact takes place between the fluid kinetic energy E_k and fluid potential energy E_p. As the wave moves up along the wall, E_p increases and E_k decreases, which leads to a reduction of the air pocket oscillation amplitudes. The duration over which the pressure oscillation decays to an insignificant level is close to 0.8, the value measured by Chan (1986).

6.4. *Maximum impact pressure on the wall*

The computed and measured maximum impact pressures on the wall are plotted in figure 19. The simulation results, figure 19(a), give the wall pressure distribution at the instant, T_r, when P_m is reached. Our simulations show that the maximum pressures in the vicinity of P_m (close to the air pocket) are also reached at approximately the same time instant. Thus the pressure profile(s) in figure 19(a) near P_m can be considered to be also the maximum wall pressures at these locations. Far from P_m, this is no longer true, and the value there should not be considered to be the maxima reached. Our main interest, of course, is in P_m and values in its vicinity.

For comparison, the measured peak pressures at seven locations from repeated runs of CM (see also Chan 1986) are plotted on the same scale in figure 19(b). Comparing the two, we note that the computed P_m (using $\gamma_a = 1.4$) is $\simeq 20.2$ which is reached at $t - t_I \simeq 0.003$ at a location of $y \simeq 0.16$. This maximum pressure is about three times ($\sim$ 4.5 standard deviations) higher than the mean measured value of the maximum wall pressure ($P_m \simeq 6$) which is obtained at approximately the same location. Away from P_m, the measured maximum values decrease rapidly with depth and are lower than those from the computed profile. Indeed, the overall qualitative comparison would be better if the computed profile(s) could be reduced (shifted) by a constant value. Returning to the quantitative comparison of P_m, it is important to take into account some of the physical factors present in the measurements.

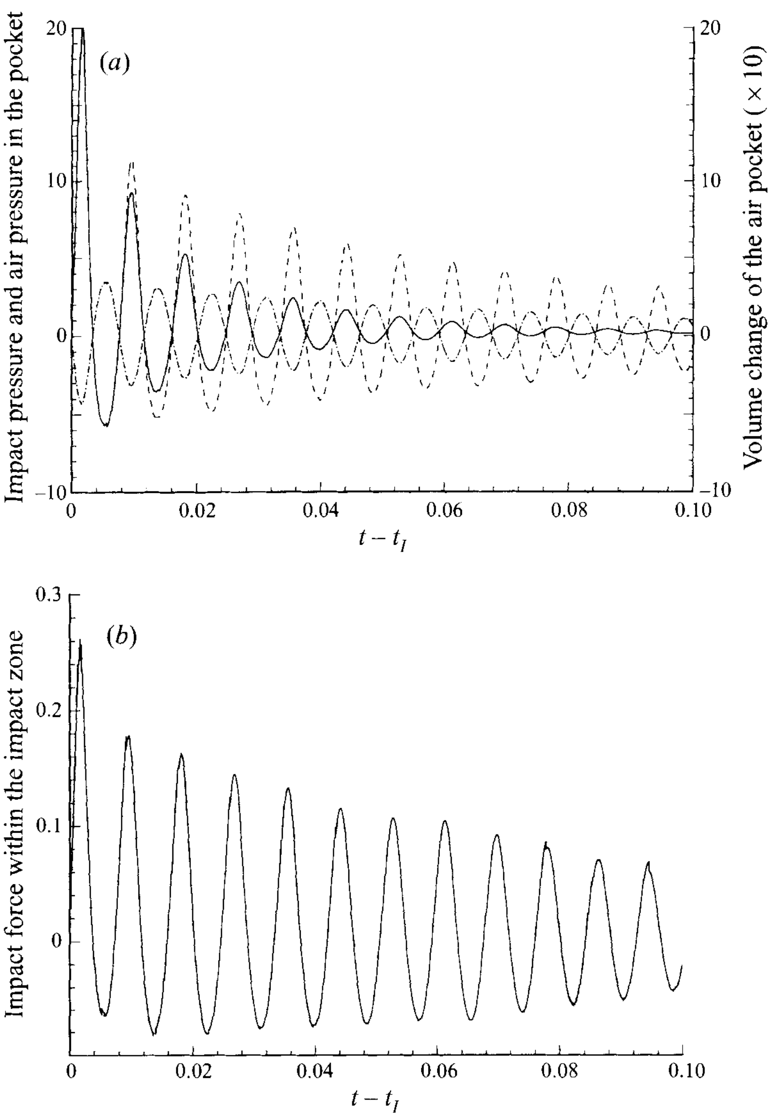

FIGURE 18. (*a*) Temporal evolution of the wall impact pressure at $y/h_0 = 0.16$ (———); the air pocket pressure variation $P_a/P_0 - 1$ (— — —); and the trapped air volume change $V_a(t)/V_a(0) - 1$ (— · — ·). (*b*) Temporal evolution of the wall impact force within the impact zone (on S_W).

Effect of spray and air leakage

In the simulations, the trapped air pocket is modelled as a two-dimensional area within a (simple) closed contour. In reality, the pocket is a region of water spray resulting from instability of the breaking wave and air entrainment. According to Schmidt *et al.* (1992), the air entrainment in a plunging breaker impact on a vertical wall can reduce the sound speed in the impact region to a mean value of ~ 210 m s^{-1}, which is about an 80% reduction of the sound speed in water. In addition to the spray effect, some of the trapped air escapes vertically along the wall during the impact. This reduces the 'stiffness' of the air pocket and consequently the maximum air pressure in the pocket and P_m as well.

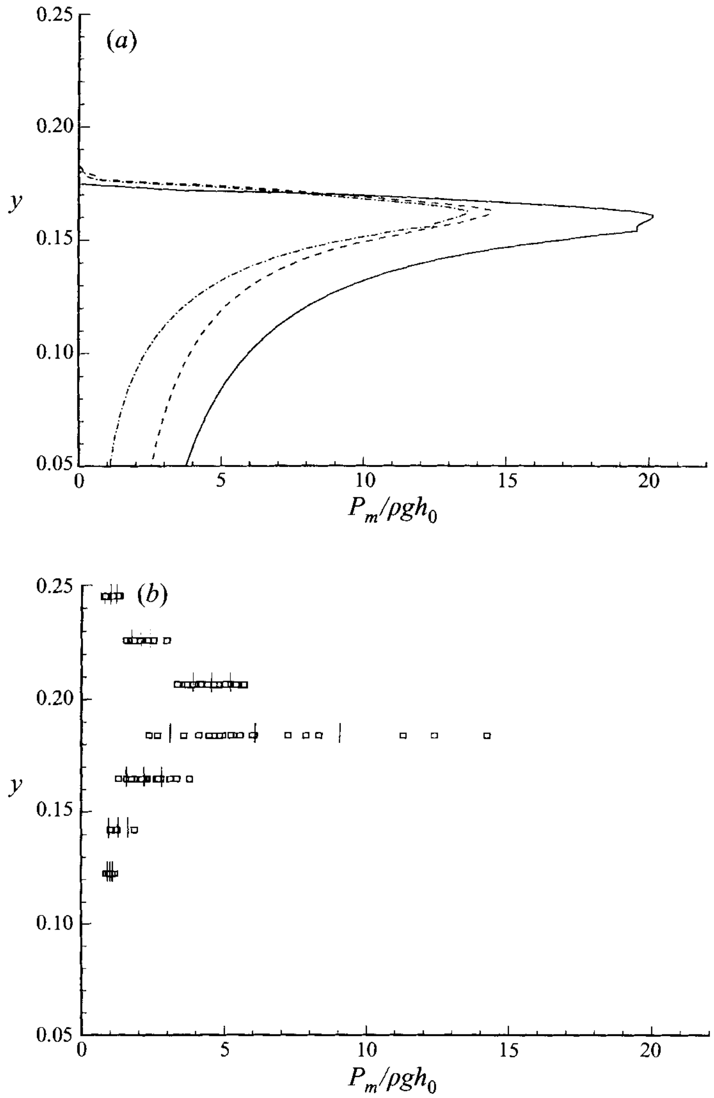

FIGURE 19. Wall impact pressure profile at the instant P_m is reached. (a) Numerical simulations for: $\gamma_a = 1.4$ (at $t - t_l = 0.003$) (——); $\gamma_a = 0.5$ (at $t - t_l = 0.004$) (— — —); and $\gamma_a = 0.5$ for an elastic wall (at $t - t_l = 0.004$) (— · — ·). (b) Experimental measurements of Chan (1986) and CM (1988) in repeated runs at seven locations. The three vertical bars indicate respectively the mean value and mean plus and minus one standard deviation of the measured values.

Such two-phase flow phenomena cannot be rigorously described in the present simulation because of lack of information of the equation of state in the trapped-air region. However, the trapped-air effect on P_m and T_r can be approximately modelled within the present framework by adjusting the global behaviour of the trapped-air pocket, in this case, the 'effective stiffness' of the air pocket. As shown in (5.8), γ_a can be treated as a spring constant in the mass–spring system. Thus, an approximate way to account for the net effects of spray and air leakage is to consider a value of γ_a that is smaller than 1.4 (Koehler & Kettleborough 1977). We remark that while modifying the value of γ_a in a polytropic law is strictly non-physical, it provides a useful mechanical interpretation (e.g. Prosperetti 1977, 1982) in the present context.

To obtain a suitable value of γ_a for comparison to experiment, two estimations are made. One is based on the relation between γ_a and the natural frequency of a spherical bubble in an unbounded fluid oscillating with respect to its initial radius R_0 and initial gas pressure P_0 (Lighthill 1978; Prosperetti 1982), $\omega_0 = (3\gamma_a P_0/\rho)^{1/2}/R_0$. From Chan (1986, p. 200), the measured frequency of the pressure oscillation due to the air pocket pulsation is about 400 Hz and the width of the (two-dimensional) pocket is 1 cm. Approximating R_0 to be 0.5 cm, a value of $\gamma_a \simeq 0.53$ is obtained. Another estimation is obtained from the measured sound speed in the plunging wave impact regions by Schmidt *et al.* (1992). Assuming that the mean measured value of the sound speed of $C \approx 210$ m s^{-1} is valid inside the air pocket (Landau & Lifshit 1979, p. 248), γ_a can be deduced from $C = (\gamma_a P_0/\rho_a)^{1/2}$ where ρ_a is the density of the air ($\rho_a/\rho \approx 0.0013$). This gives $\gamma_a \simeq 0.57$.

Based on the above argument, a new simulation is performed using a value of $\gamma_a = 0.5$ for the trapped air. The resulting wall pressure profile for P_m is also plotted in figure 19(*a*). In this case, the maximum impact pressure is $P_m \simeq 14.52$ at $y \simeq 0.16$ and is reached at $t - t_I \simeq 0.004$. This represents approximately a 28% reduction in P_m compared to the case of $\gamma_a = 1.4$.

Effect of hydroelasticity

In the simulations, the vertical wall is considered to be rigid, which tends to overestimate the resulting maximum pressure compared to the more realistic case of a (stiff) elastic wall (e.g. Kirkgöz 1990; Kvålsvold & Faltinsen 1995). In the experiments, Chan (1986, p. 209) indicates that the impact causes a certain degree of vibration of the vertical wall. At two locations on the wall, $y = 0.144$ and 0.1, the acceleration of the wall and the maximum perturbation pressures due to wall vibration are measured to be ~ 3g and ~ 1.2 kPa, respectively. This corresponds to a 3% ~ 6% reduction of the impact pressure compared to a rigid wall.

To investigate the hydroelastic effect, the simulation is repeated with the rigid wall replaced by a cantilever elastic elementary beam. From the experiment, the material properties are estimated to be mass per unit area ≈ 0.175 and flexural rigidity ≈ 0.01. Again a value of $\gamma_a = 0.5$ is used. In the hydroelastic simulation, the fluid motion during impact is coupled with the response of the beam (cf. Zhang, Storhaug & Yue 1995). The resulting profile of the maximum wall pressure is also plotted in figure 19(*a*). The maximum pressure P_m is now reduced by ~ 6% to a value of 13.63. The maximum impact force on the wetted area S_W is reduced by ~ 8% from 0.206 for the rigid wall to 0.189 for the elastic wall.

Effect of size and spacing of the pressure transducers

The spacing and sensing size of the pressure transducers in the experiment directly affect the peak pressure measurement (Takemoto 1984; Führböter 1986). The distance between two adjacent pressure transducers in CM is ≈ 0.02, while the transducer diameter itself is ≈ 0.01. Using the wall pressure profiles in figure 19, we estimate reductions in the measured value of P_m in the range of 1~3 depending on the location of P_m relative to the probes.

Taking all of the above effects into account, the best numerical estimation of the value of $P_m/\rho U^2$ to be compared with the measurements of CM is between 10.63 and 12.63 with a mean value of 11.63. This is shown in figure 19 compared to measured maximum impact pressures at seven locations along the wall in repeated experiments by Chan (1986) (cf. CM figures 16 and 17). The mean value of P_m registered by the transducer located at $y = 0.184$ from 21 measurements is 6.18 with a standard deviation of 3.11. The difference between the mean value of the calculated maximum pressure (using $\gamma_a = 0.5$ and accounting for hydroelasticity and reductions due to discrete transducer measurements) and the mean experimental value is thus approximately 1.75 standard deviations of the experiments.

The maximum pressure rise time T_r from the calculation for $\gamma_a = 0.5$ is 0.0039, while the mean value of T_r from the experiments is 0.0047 with a standard deviation of 0.0022. The difference in T_r between the calculation and the experiment is therefore less than 0.4 measurement standard deviations. Given the large sensitivity and variability in the experiment, such comparisons for P_m and T_r are quite remarkable.

It is remarked finally that if the experimental parameters of CM are used directly in the scaling law in §5 (with $C_P = 2.6$ and $C_T = 0.73$, respectively), the predicted P_m is 14.6 (before adjusting for wall elasticity and transducer reductions) as compared to the corresponding value of 14.5 for $\gamma_a = 0.5$ and 20.2 for $\gamma_a = 1.4$ given above. The corresponding scaling law prediction for T_r is 0.0021.

7. Conclusion

The impact of a two-dimensional plunging breaking wave trapping an air pocket against a vertical wall is studied numerically. The plunging wave generated by a piston wavemaker is simulated using a mixed-Eulerian–Lagrangian (MEL) boundary-integral scheme. The initial stage of the impact is characterized by an oblique impact of a liquid wedge on the wall and described by a similarity solution. Following the initial impact, the simulation with a trapped air pocket is continued using MEL with the trapped air described by a polytropic gas law. The focus of the study is on the maximum impact pressure on the wall and the scaling law valid for the present case of impact involving trapped air.

The major results of this study are as follows. The maximum wall impact pressure can be well scaled by the local parameters of the breaker at the instant of impact: U, the horizontal impact velocity; h, the depth of the plunger tip; ℓ and H, the width and height of the air cushion; and P_0 the initial air pocket pressure (atmospheric pressure). Among these, the dimensionless parameters $P_0/\rho U^2$ and ℓ/h are found to be most important, and provide the scaling laws for the maximum impact pressure, $P_m/\rho U^2$, and the rise time of this pressure, $T_r U/(H\ell)^{1/2}$, based on a simplified spring–mass model of the impact process. Systematic MEL simulations (sixty in all) varying these parameters support this model and provide best-fit estimates of the model coefficients.

As a practical illustration, simulations are performed and direct quantitative comparisons are made to the tank experiment of Chan & Melville (1988). The present numerical simulations compare quantitatively with the experimental measurements of CM, especially when experimental/physical factors not present in the computational model are accounted for. The predictions for this case based on the simple scaling laws we derived are also reasonably good. These provide support for the validity and usefulness of MEL simulations for practical predictions and for the reliability of the scaling laws we obtained.

This work was supported financially by grants from the Office of Naval Research.

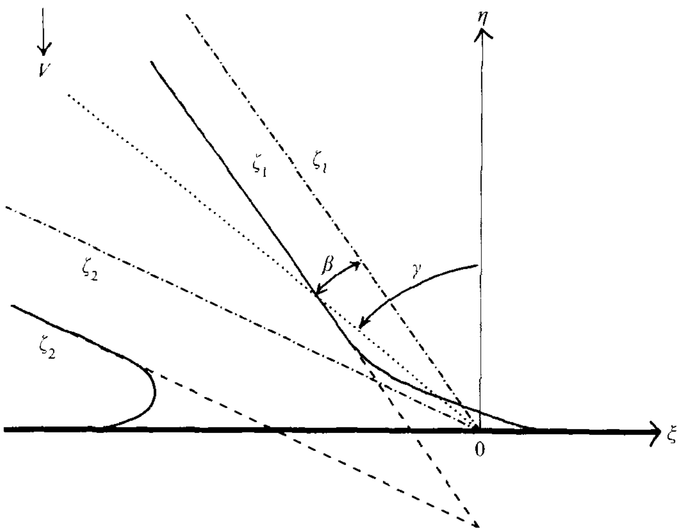

FIGURE 20. Definition sketch in the similarity-variable plane (ξ,η) for the non-symmetric normal impact of a liquid wedge on a rigid wall at the instant of impact (— · — ·); shortly after impact (——) (the matched similarity profile); and the profile in the absence of the wall (- - - -).

Appendix A. Similarity solution for the non-symmetric normal impact of a liquid wedge on a wall

Introducing similarity variables $\xi = x/Vt$, $\eta = y/Vt$, $\Phi = \phi/V^2t$ and $\zeta_i = S_i/Vt$, i=1,2, into (3.1) to (3.5) (with $U = 0$), the following equations in the similarity plane (ξ,η) (see figure 20) are obtained:

$$\nabla^2\Phi(\xi,\eta) = 0 \quad \text{in} \quad D(\xi,\eta), \tag{A 1}$$

$$\frac{\partial\Phi}{\partial\eta} = 0 \quad \text{on} \quad \eta = 0, \tag{A 2}$$

$$\nabla\Phi = -\boldsymbol{j} \quad \text{at} \quad \infty, \tag{A 3}$$

$$\frac{\partial\Phi}{\partial\xi} = \zeta_i - \eta\frac{\mathrm{d}\zeta_i}{\mathrm{d}\eta} + \frac{\partial\Phi}{\partial\eta}\frac{\mathrm{d}\zeta_i}{\mathrm{d}\eta} \quad \text{on} \quad \xi = \zeta_i(\eta), \tag{A 4}$$

$$\Phi - \xi\frac{\partial\Phi}{\partial\xi} - \eta\frac{\partial\Phi}{\partial\eta} + \frac{1}{2}\left[\left(\frac{\partial\Phi}{\partial\xi}\right)^2 + \left(\frac{\partial\Phi}{\partial\eta}\right)^2\right] = 0 \quad \text{on} \quad \xi = \zeta_i(\eta). \tag{A 5}$$

Letting $\partial\Phi/\partial\xi\,|_{\xi=\zeta_i(\eta)} = u_i(\eta)$ and $\partial\Phi/\partial\eta\,|_{\xi=\zeta_i(\eta)} = v_i(\eta)$, and differentiating (A 5) with respect to η, the boundary conditions (A 4) and (A 5) can be expressed as

$$(v_i - \eta)v_i' + (u_i - \zeta_i)u_i' = 0, \tag{A 6}$$

$$u_i = \zeta_i - \eta\zeta_i' + v_i\zeta_i', \tag{A 7}$$

where $'$ represents the derivative with respect to η. Eliminating u_i from (A 6) yields

$$v_i' = \frac{(\eta - v_i)\zeta_i'\zeta_i''}{1 + \zeta_i'^2}. \tag{A 8}$$

It is noted that (A 8) is a first-order ordinary equation for $v_i(\eta)$ provided that the free-surface profiles ζ_i are known. Now assuming ζ_i are linear functions of η away from the wall and exponential functions of η near the wall (Borisova *et al.* 1959), ζ_i can be written as

$$\zeta_i = a_i\eta + b_i + d_i\mathrm{e}^{-c_i\eta}, \tag{A 9}$$

where a_i, b_i, c_i and d_i are constants to be determined. As $\eta \to \infty$, $\zeta_i \to (\eta+1)\tan\alpha_i$ with $\alpha_1 = \gamma+\beta$ and $\alpha_2 = \gamma-\beta$. This produces $a_i = b_i = \tan\alpha_i$. To find the remaining four unknowns c_i and d_i, (A 9) is substituted into (A 8) and upon solving (A 8) the expressions for v_i are obtained:

$$v_i = \frac{C_0}{\mu_i} + \left(1-\frac{\lambda_i}{\mu_i}\right)\eta + \frac{1}{c_i} - \frac{a_ie_i}{c_i\mu_i}\ln 2c_id_ie_i\left(\mu_i - \zeta_i'e_i\right) - \frac{\lambda_i}{c_i\mu_i}\ln 2(\lambda_i\mu_i + a_i\zeta_i' + 1), \tag{A 10}$$

where $\lambda_i = (1+a_i^2)^{1/2}$, $\mu_i = (1+\zeta_i'^2)^{1/2}$, e_i =sign(d_i) and C_0 is a constant. Using boundary conditions $v_i|_{\eta=0} = 0$ and $v_i|_{\eta\to\infty} = -1$ to eliminate C_0 in (A 10) yields

$$\begin{aligned}\frac{1}{c_i}\left(1-\frac{\lambda_i}{h_i}\right) - \frac{\lambda_i}{h_i} + \frac{a_ie_i}{c_ih_i}\ln\left[\frac{\lambda_i - a_ie_i}{4\lambda_i^2(h_i - a_ie_i + c_id_ie_i)}\right]&\\ -\frac{\lambda_i}{c_ih_i}\ln 2[\lambda_ih_i + a_i(a_i - c_id_i) + 1] = 0,&\end{aligned} \tag{A 11}$$

where $h_i^2 = 1 + (a_i - c_id_i)^2$.

With $i = 1, 2$, (A 11) gives two independent relations. To solve for c_i and d_i, two more equations are needed. Considering the conservation of mass (see figure 20), the fluid volume displaced by the wall should equal that passing the wall position if the wall were absent. Thus, the area of the triangle enclosed by the wedge and the wall should be identical to the areas enclosed by the free surfaces ζ_i, and the wall and the edges of the wedge at $t = 0$ given by $\bar{\zeta}_i = a_i\eta + b_i$. The expression for the conservation of mass has the form

$$\int_0^\infty |\zeta_1 - \bar{\zeta}_1|\mathrm{d}\eta + \int_0^\infty |\zeta_2 - \bar{\zeta}_2|\mathrm{d}\eta = \tfrac{1}{2}(a_1 - a_2), \tag{A 12}$$

which yields the third relation

$$\frac{d_1}{c_1} - \frac{d_2}{c_2} = \tfrac{1}{2}(a_1 - a_2). \tag{A 13}$$

Now considering the conservation of momentum in the direction parallel to the wall, the fluid momentum in the ξ-direction should be a constant since an impact in the η-direction does not change the momentum in the ξ-direction. This implies that the ξ-momentum of the fluid after the fluid is displaced by the wall is equal to that of the fluid if the wall were absent. This relation can be written as

$$\begin{aligned}\int_0^\infty [\zeta_1(\zeta_1 - \eta\zeta_1') - \bar{\zeta}_1(\bar{\zeta}_1 - \eta\bar{\zeta}_1')\mathrm{d}\eta - \int_0^\infty [\zeta_2(\zeta_2 - \eta\zeta_2') - \bar{\zeta}_2(\bar{\zeta}_2 - \eta\bar{\zeta}_2')]\mathrm{d}\eta&\\ = \int_{-1}^0 [\bar{\zeta}_1(\bar{\zeta}_1 - \eta\bar{\zeta}_1') - \bar{\zeta}_2(\bar{\zeta}_2 - \eta\bar{\zeta}_2')]\mathrm{d}\eta.&\end{aligned} \tag{A 14}$$

This produces the fourth relation for c_i and d_i,

$$\frac{3}{4}\left(\frac{d_1^2}{c_1} - \frac{d_2^2}{c_2}\right) + \frac{3a_1d_1}{c_1}\left(\frac{1}{c_1} + 1\right) - \frac{3a_2d_2}{c_2}\left(\frac{1}{c_2} + 1\right) = \tfrac{1}{2}(a_1^2 - a_2^2). \tag{A 15}$$

Equations (A 11), (A 13) and (A 15) form a system of nonlinear algebraic equations for c_i and d_i which can be formally represented as $\boldsymbol{F}(\boldsymbol{X}) = 0$ with $\boldsymbol{X} = (c_1, c_2, d_1, d_2)$. The solution can be obtained by Newton iteration: $\Delta X_k = -\nabla F^{-1}(X_k)F(X_k)$ and

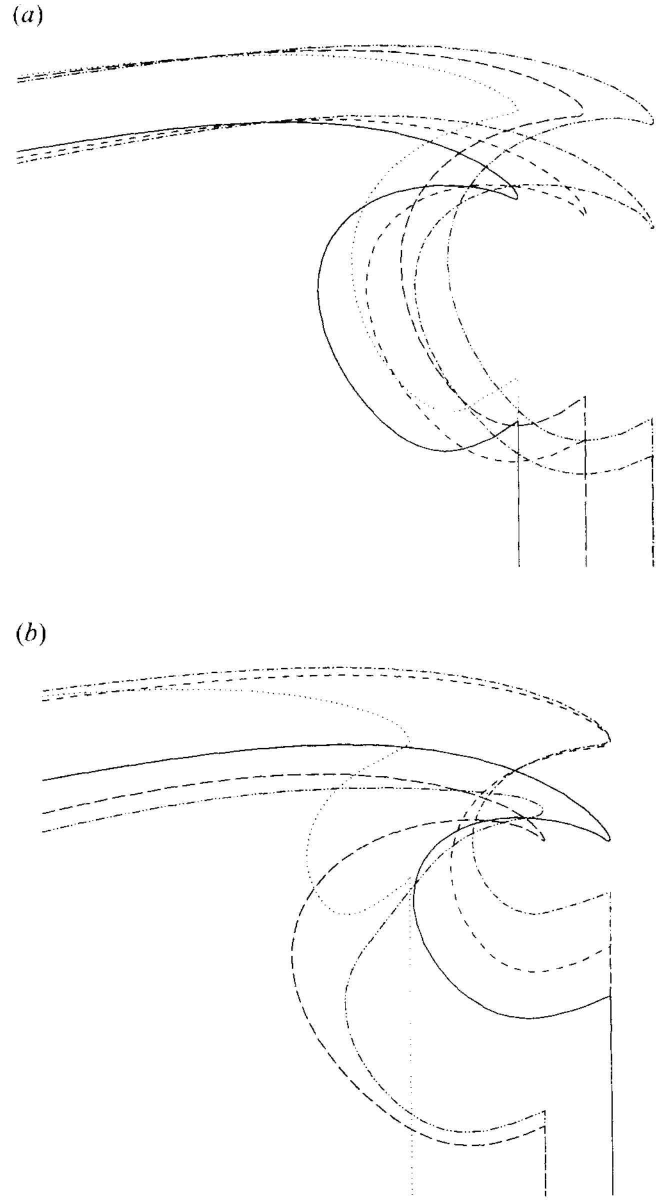

FIGURE 21. Free-surface profiles at the time of impact for the twelve cases in Appendix B. (*a*) Cases 1 (——), 2 (- - - -), 3 (— · — ·), 4 (· · · ·), 5 (— — —), 6 (— · · —); and (*b*) cases 7 (——), 8 (- - - -), 9 (— · — ·), 10 (· · · ·), 11 (— — —) and 12 (— · · —).

$X_{k+1} = X_k + \Delta X_k$, where k is the iteration index and ∇ is the gradient operator with respect to X. The initial guess for X is chosen as $(2, 2, 1, -1)$. The increment ΔX is obtained iteratively until the solution converges to $||\Delta X||_\infty < 10^{-8}$.

Substituting the values of a_i, b_i, c_i, and d_i into (A 9) gives the free-surface profiles ζ_i. The velocity of the free surfaces is given by (A 7) and (A 10). The pressure on the wetted area, S_W, can be calculated numerically by solving a boundary-value problem for ϕ on S_W with Dirichlet boundary conditions on S_i and S_∞ given by the similarity solution.

Case	L_0	U_0	h_e	L_1	ℓ	ℓ/H	ℓ/h	ℓ/H_b	U
1	5.6	0.7	0.5	3.0	0.301	0.628	3.308	0.287	1.895
2	5.7	0.7	0.5	3.0	0.328	0.659	3.814	0.314	1.898
3	5.8	0.7	0.5	3.0	0.355	0.689	4.128	0.339	1.912
4	5.6	0.8	0.5	3.2	0.250	0.498	1.923	0.212	2.016
5	5.7	0.8	0.5	3.2	0.276	0.520	2.140	0.233	2.034
6	5.8	0.8	0.5	3.3	0.306	0.543	2.488	0.258	2.066
7	5.7	0.7	0.4	3.0	0.294	0.797	3.231	0.281	1.909
8	5.7	0.8	0.4	3.2	0.238	0.617	1.935	0.201	2.052
9	5.7	0.8	0.3	3.2	0.206	0.720	1.776	0.174	2.066
10	5.4	0.8	0.4	3.1	0.155	0.601	1.314	0.133	1.987
11	5.6	0.7	0.5	2.5	0.378	0.651	4.909	0.368	1.859
12	5.6	0.8	0.5	2.5	0.298	0.587	2.423	0.294	1.741
*	11.75	$f(t)$	0.0	0.0	0.013	1.182	1.625	0.077	1.369

TABLE 1. L_0, initial tank length at $t = 0$; U_0, horizontal velocity of the wave maker; h_e, depth of the exit channel under the vertical wall; L_1, distance at which the wave maker stops moving; ℓ, thickness of the air pocket (see figure 10); H, depth of the air pocket (see figure 10); h, depth of the plunger (see figure 10); H_b, height of the plunger measured from the plunger crest to the still-water level; U, horizontal impact velocity of the plunger tip at the instant of impact.

Appendix B. Characteristics of the numerically generated plunging breakers

Table 1 summarizes the characteristics of the plunging breakers used in the numerical simulations in §4, §5 and §6. The free-surface profiles at the instant of impact corresponding to cases 1–12 are presented in figure 21. Case * corresponds to the experiment of CM with measured wave maker velocity history $f(t)$ (cf. Dommermuth *et al.* 1988).

REFERENCES

BAGNOLD, R. A. 1939 Interim report on wave pressure research. *J. Inst. Civ. Engng* June, 202–226.

BLACKMORE, P. A. & HEWSON, P. J. 1984 Experiments on full-scale wave impact pressures. *Coastal Engng* **8**, 331–346.

BORISOVA, E. P., KORIAVOV, P. P. & MOISEEV, N. N. 1959 Plane and axially symmetrical similarity problems of penetration and of stream impact. *J. Appl. Math. Mech.* **23**, 490–507.

CARRIER, G. F., KROOK, M. & PEARSON, C. E. 1966 *Functions of a Complex Variable*. McGraw-Hill.

CHAN, E. S. 1986 Deep-water breaking wave forces on structures. ScD thesis, Massachusetts Institute of Technology.

CHAN, E. S. 1994 Mechanics of deep water plunging-wave impacts on vertical structures. *Coastal Engng* **22**, 115–133.

CHAN, E. S. & MELVILLE, W. K. 1988 Deep-water plunging wave pressure on a vertical plane wall. *Proc. R. Soc. Lond.* A **417**, 95–131 (referred to herein as CM).

COLE, R. H. 1948 *Underwater Explosions*. Princeton University Press.

COOKER, M. J. & PEREGRINE, D. H. 1991 Wave breaking and wave impact pressures. In *Development in Coastal Engineering* (ed. D. H. Peregrine & J. Loveless), pp. 47–64. University of Bristol.

COOKER, M. J. & PEREGRINE, D. H. 1992 Wave impact pressure and its effect upon bodies lying on the sea bed. *Coastal Engng* **18**, 205–229.

COOKER, M. J. & PEREGRINE, D. H. 1995 Pressure-impulse theory for liquid impact problems. *J. Fluid Mech.* **297**, 193–214.

CUMBERBATCH, E. 1960 The impact of a water wedge of a wall. *J. Fluid Mech.* **7**, 353–374.

DOBROVOL'SKAYA, Z. N. 1969 On some problems of similarity flow of fluid with a free surface. *J. Fluid Mech.* **34**, 805–829.

DOLD, J. W. & PEREGRINE, D. H. 1986 An efficient boundary-integral method for steep unsteady water waves. On some problems of similarity flow of fluid with a free surface. *Numerical*

Methods for Fluid Dynamics II (ed. K. W. Morton, & M. J. Baines), pp. 671–679. Oxford University Press.

Dommermuth, D. G., Yue, D. K. P., Lin, W. M., Rapp, R. J., Chan, E. S. & Melville, W. K. 1988 Deep-water plunging breakers: a comparison between potential theory and experiments. *J. Fluid Mech.* **189**, 423–442.

Führböter, A. 1986 Model and prototype tests for wave impact and run-up on a uniform 1:4 slope. *Coastal Engng* **10**, 49–84.

Hattori, M., Arami, A. & Yui T. 1994 Wave impact pressure on vertical walls under breaking waves of various types. *Coastal Engng* **20**, 79–114.

Hayashi, T. & Hattori, M. 1958 Pressure of the breaker against a vertical wall. *Coastal Engng in Japan* **1**, 25–37.

Kirkgöz, M. S. 1990 An experimental investigation of a vertical wall response to breaking wave impact. *Ocean Engng* **17**, 379–391.

Kirkgöz, M. S. 1991 Impact pressure of breaking waves on vertical and sloping walls. *Ocean Engng* **18**, 45–59.

Koehler, Jr. B. R. & Kettleborough, C. F. 1977 Hydrodynamic impact of a falling body upon a viscous incompressible fluid *J. Ship Res.* **21**, 165–181.

Korobkin, A. A. & Pukhnachov, V. V. 1988 Initial stage of water impact. *Ann. Rev. Fluid Mech.* **20**, 159–185.

Kvålsvold, J. & Faltinsen, O. M. 1995 Hydroelastic modelling of wet deck slamming on multihull vessels. *J. Ship Res.* **39**, 225–239.

Lamb, H. 1932 *Hydrodynamics*. Cambridge University Press.

Landau, L. D. & Lifshit, E. M. 1979 *Fluid Mechanics*. Pergamon Press.

Lighthill, J. 1978 *Waves in Fluids*. Cambridge University Press.

Lundgren, H. 1969 Wave shock forces: an analysis of deformations and forces in the wave and in the foundation. *Proc. Symp. on Research in Wave Action, Delft Hydraulic Laboratory, Delft, The Netherlands*, Paper 4.

Miller, R. L., Leverette, S. & O'Sollivan, J. 1974 Field measurements of impact pressures in surft, *Proc. 14th Int. Conf. Coastal Engng* vol. 3, pp. 1761–1777.

Mitsuyasu, H. 1966 Shock pressure of breaking wave. *Proc. 10th Intl Conf. Coastal Engng Tokyo*, pp. 268–283.

Ochi, M. K. & Tsai, C. H. 1984 Prediction of impact pressure induced by breaking waves on vertical cylinders in random seas. *Appl. Ocean Res.* **6**, 157–165.

Oumeraci, H., Klammer, P. & Partenscky, H. W. 1993 Classification of breaking wave loads on vertical structures. *J. Waterway, Ports, Coastal, and Ocean Eng.* **119**, 4, 381–397.

Press, H. W., Flannery, B. P., Tenkolsky, S. A. & Vetteling, W. T. 1989 *Numerical Recipes*. Cambridge University Press.

Prosperetti, A. 1977 Thermal effects and damping mechanisms in the forced radial oscillations of gas bubbles in liquids. *J. Acoust. Soc. Am.* **61**, 17–27.

Prosperetti, A. 1982 Bubble dynamics: a review and some recent results. *Appl. Sci. Res.* **38**, 145–164.

Schmidt, R., Oumeraci, H. & Partenscky, H. W. 1992 Impact loads induced by plunging breakers on vertical structures. *Proc. 23rd Intl Conf. Coastal Engng ASCE, Venice*, pp. 1545–1558.

Stive, R. J. H. 1984 Wave impact on uniform steep slopes at approximately prototype scale. *Symp. on Scale Effects in Modelling Hydraulic Structures, Esslingen am Neckar, Germany* (ed. H. Kobus), pp. 7.11-1–11.7.

Takemoto, H. 1984 Water impact test of a wedge with rectangular plates and its analysis. *J. Soc. Naval Arch. Japan* **156**, 306–313.

Tanizawa, K. & Yue, D. K. P. 1991 Numerical computation of plunging wave impact loads on a vertical wall. *Proc. 6th Intl Workshop on Water Waves & Floating Bodies, WHOI, MA, USA.*

Tanizawa, K. & Yue, D. K. P. 1992 Numerical computation of plunging wave impact loads on a vertical wall. *Proc. 7th Intl Workshop on Water Waves & Floating Bodies, France.*

Taylor, P. W. 1990 Fully-nonlinear simulation of a plunging breaking wave impacting a vertical wall. Master thesis, MIT.

Topliss, M. E. 1994 Water wave impact on structures. PhD thesis, School of Mathematics, University of Bristol.

VINJE, T. & BREVIG, P. 1980 Numerical simulation of breaking waves. *3rd Intl Conf. Finite Elements Water Resources*, University of Missouri.

VINJE, T. & BREVIG, P. 1981 Numerical calculation of forces from breaking waves. *Proc. Intl Symp. Hydro. Ocean Engng, Trondheim, Norway.*

WANG, Y. F. & SU, T. C. 1992 Numerical simulation of breaking waves against vertical wall. *Proc. 2nd Intl Offshore & Polar Eng. Conf. San Francisco, USA*, pp. 14–19.

WHILLOCK, A. F. 1987 Measurements of forces resulting from normal and oblique wave approaches to small scale sea walls. *Coastal Engng* **11**, 297–308.

WHITMAN, A. M. & PANCIONE, M. C. 1973 A similitude relation for flat-plate hydrodynamic impact. *J. Ship Res.* 38–42.

ZHANG, S. STORHAUG, G. & YUE, D. K. P. 1995 Wave loads on a vertical elastic wall. *Proc. 10th Intl Workshop on Water Waves & Floating Bodies, Oxford, UK.*

ZHAO, R. & FALTINSEN, O. 1993 Water entry of two-dimensional bodies. *J. Fluid Mech.* **246**, 593–612.